Marine and Petroleum Geology 112 (2020) 104080

Contents lists available at ScienceDirect

Marine and Petroleum Geology

journal homepage: www.elsevier.com/locate/marpetgeo

Research paper

Hot fluids, burial metamorphism and thermal histories in the underthrust sediments at IODP 370 site C0023, Nankai Accretionary Complex

Man-Yin Tsang[a,1], Stephen A. Bowden[b,*,1], Zhibin Wang[b], Abdalla Mohammed[b], Satoshi Tonai[c], David Muirhead[b], Kiho Yang[d], Yuzuru Yamamoto[e], Nana Kamiya[f], Natsumi Okutsu[g], Takehiro Hirose[h], Myriam Kars[i], Florence Schubotz[j], Akira Ijiri[h], Yasuhiro Yamada[c,k,l], Yusuke Kubo[h,l], Yuki Morono[h], Fumio Inagaki[m], Verena B. Heuer[j], Kai-Uwe Hinrichs[j]

[a] Department of Earth Sciences, University of Toronto, 22 Russell Street, Toronto, ON M5S 3B1, Canada
[b] School of Geosciences, University of Aberdeen, Aberdeen AB2A 3UE, UK
[c] Department of Natural Science, Kochi University, 2-5-1 Akebono-cho, Kochi 780-8520, Japan
[d] Korea Institute of Ocean Science and Technology, Uljin 767-813, South Korea
[e] Department of Mathematical Science and Advanced Technology, Japan Agency for Marine Earth Science and Technology, 3173-25 Showa-machi, Kanazawa-ku, Yokohama Kanagawa 236-0001, Japan
[f] Department of Urban Management, Kyoto University, C1-1-118 C-cluster, Kyoto Daigaku Katsura, Nishikyo-ku, Kyoto, 615-8540, Japan
[g] Atmosphere and Ocean Research Institute, The University of Tokyo, 5-1-5 Kashiwanoha, Kashiwa, Chiba 277-8564, Japan
[h] Kochi Institute for Core Sample Research, Japan Agency for Marine Earth Science and Technology, Monobe B200, Nankoku, Kochi 783-8502, Japan
[i] Center for Advanced Marine Core Research, Kochi University, B200 Monobe, Nankoku, Kochi 783-8502, Japan
[j] MARUM-Center for Marine Environmental Sciences, University Bremen, Leobener Strasse 8, 28359 Bremen, Germany
[k] Research and Development Center for Ocean Drilling Science, Japan Agency for Marine-Earth Science and Technology, 3173-25, Showa-machi, Kanazawa, Yokohama, 236-0001, Japan
[l] Center for Deep Earth Exploration (CDEX), Japan Agency for Marine-Earth Science and Technology, 3173-25, Showa-machi, Kanazawa, Yokohama, 236-0001, Japan
[m] Mantle Drilling Promotion Office, Institute for Marine-Earth Exploration and Engineering, Japan Agency for Marine-Earth Science and Technology, Showa-machi 3173-25, Kanazawa-ku, Yokohama 236-0001, Japan

ARTICLE INFO

Keywords:
Hot fluids
Biomarkers
Hydrothermal mineralization
Fluid inclusions
IODP 370 temperature limits
International Ocean Discovery Program

ABSTRACT

Drilling during International Ocean Discovery Program (IODP) Expedition 370 at Site C0023 encountered instances of hydrothermal mineralization from 775 to 1121 m below seafloor. Fluid inclusion homogenization temperatures measured on barite veins within this interval indicate precipitation from fluids with temperatures up to 220 °C, and salinities ten times higher than interstitial water (16–25 c.f. 2.8–3.6 wt % NaCl). Patches of stratabound mineralization (rhodochrosite, calcite, barite and anhydride) are largely confined to the vicinity of veins and have vertical thicknesses and extents that can be explained by precipitation within the thermal aureoles of veins. Thermal maturities measured on petroleum biomarkers in underthrust sediments record a rise from pre-oil window to early oil window thermal maturities. Basin models show that increases in thermal maturity can be explained by burial metamorphism, and kinetic-based calculations suggest that hot fluids would only have had a minimal effect on hydrocarbon generation. However, the movement of hot fluids still has geochemical implications and creates a complex thermal history where both short-duration, localized heating within fracture zones at hot temperatures (~200 °C for less than 1 yr) and heating during burial over long durations (80–110 °C for 0.5–2 Myrs) need to be considered.

1. Introduction

The seaward end of the Nankai Accretionary Complex is one of the localities where it has been suggested that catagenesis (thermal breaking of carbon-carbon bonds) in hot sediments may provide electron donors to support deep microbial communities (Horsfield et al., 2006). Within the Nankai Accretionary Complex and some similar hot sedimentary settings, indicators of the presence of microbial communities including cell counts have been observed to "revive" as temperatures approach conditions under which organic substrates can

* Corresponding author.
E-mail address: s.a.bowden@abdn.ac.uk (S.A. Bowden).
[1] These two authors contributed equally on this manuscript.

https://doi.org/10.1016/j.marpetgeo.2019.104080
Received 24 June 2019; Received in revised form 7 October 2019; Accepted 8 October 2019
Available online 11 October 2019

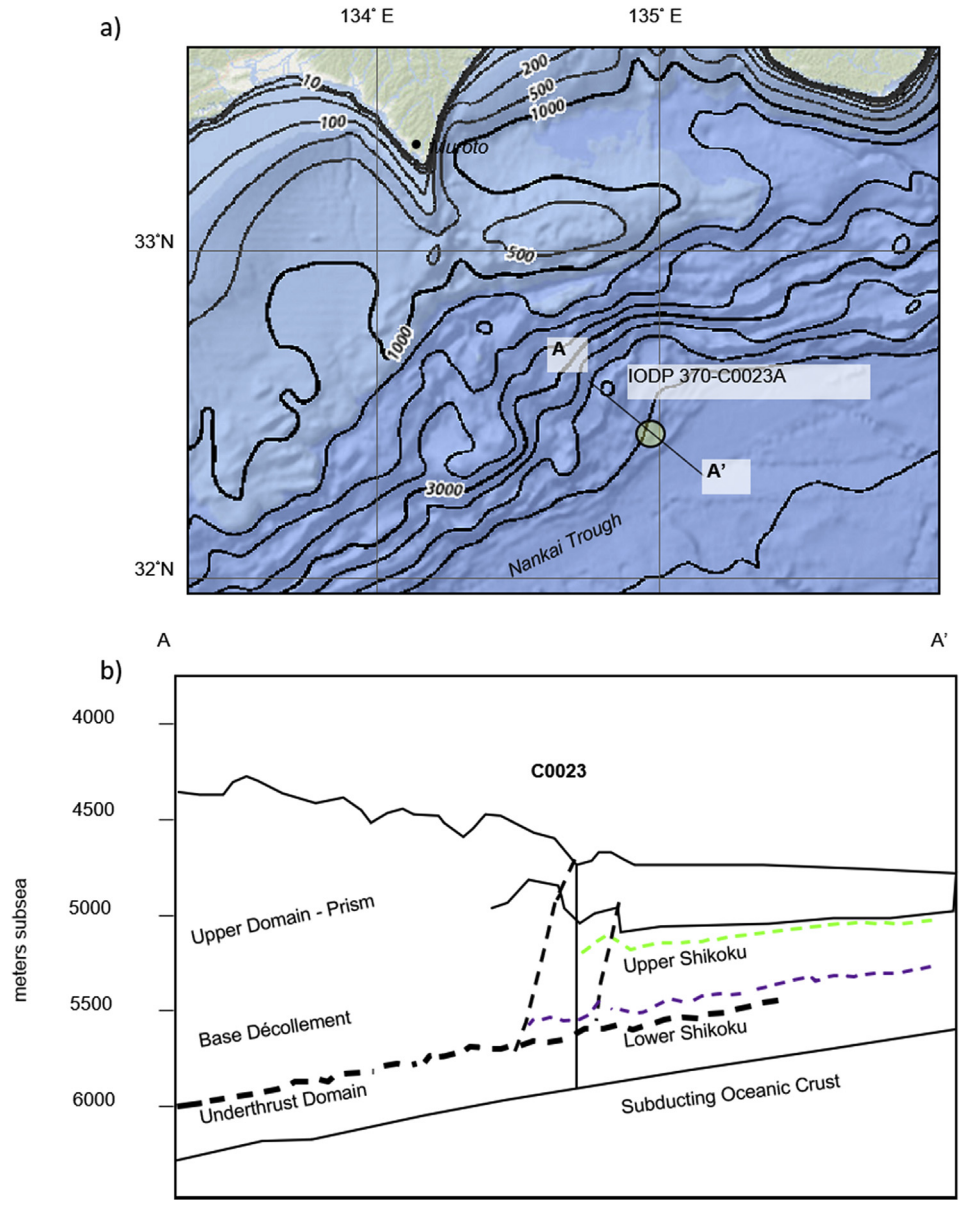

Fig. 1. a) Map and b) cross-section providing context for the Nankai Accretionary Complex. Cross-section A-A′ redrawn from the seismic section in Heuer et al. (2017). Shown are formation tops for the Upper (green) and Lower (purple) Shikoku Basin formations, and the base of the décollement zone. (For interpretation of the references to color in this figure legend, the reader is referred to the Web version of this article.)

be generated from refractory organic matter (Wellsbury et al., 1997). International Ocean Discovery Program (IODP) Expedition 370 drilled the seaward end of the Nankai Accretionary Complex (Site C0023) to the basement (120 °C) with the aim of investigating the role of temperature in controlling subseafloor life (Heuer et al., 2017, Fig. 1). This makes the determination of paleothermal regimes crucial for geobiologists studying the evolution of the deep biosphere at Site C0023. Here we present paleothermal histories based on hydrothermal mineralization as well as the general effects of burial metamorphism.

IODP Expedition 370 drilled a single site, Site C0023, and penetrated the accretionary prism, its underthrust sediments and the oceanic crust at the Nankai Trough (Fig. 1; Heuer et al., 2017). The sediments encountered within the region follow previously established descriptions: 1) from 16 Ma to 0.7 Ma, the Shikoku Basin Formation was deposited: a succession of hemipelagic mudstones and tuffs, 500 m thick and 2) from 0.7 Ma to the present day, a 600 m thick succession of turbidite deposited sandstones, siltstones and hemipelagic mudstones accumulated (Taira and Ashi, 1993). Although not as deformed as the landward part of the prism, detachment surfaces are present and bisect the Shikoku Basin facies (Aoki et al., 1982) into two separate domains: 1) an upper domain that comprises the prism, cut by low angle thrusts, 2) and an underthrust domain with extensional faulting (Figs. 1 and 2).

Despite the onset of diagenetic reactions at relatively shallow depths, and the implications this has for hot fluids, mineralization associated with hydrothermal activity had not been widely reported at the Nankai Accretionary Complex (Taira et al., 1991; Kastner et al., 1993; Moore et al., 2001). Anomalous Ca, Mg, Fe and Mn contents have been reported within sediments at nearby sites (Underwood et al., 1993) as well as anomalies of rare earth elements (Alexander et al., 1999), and these were interpreted as umbers, implying a process typically associated with the end of rifting and low-temperature off-axis activity (Pritchard and Maliotis, 1995). Umbers are ferruginous horizons found adjacent to oceanic basement, and common to the upper sections of ophiolites (Robertston, 1975) where enrichment in metal oxides imparts a distinctive coloration. However, as we will demonstrate, while ferruginous zones analogous to umbers are present at Site

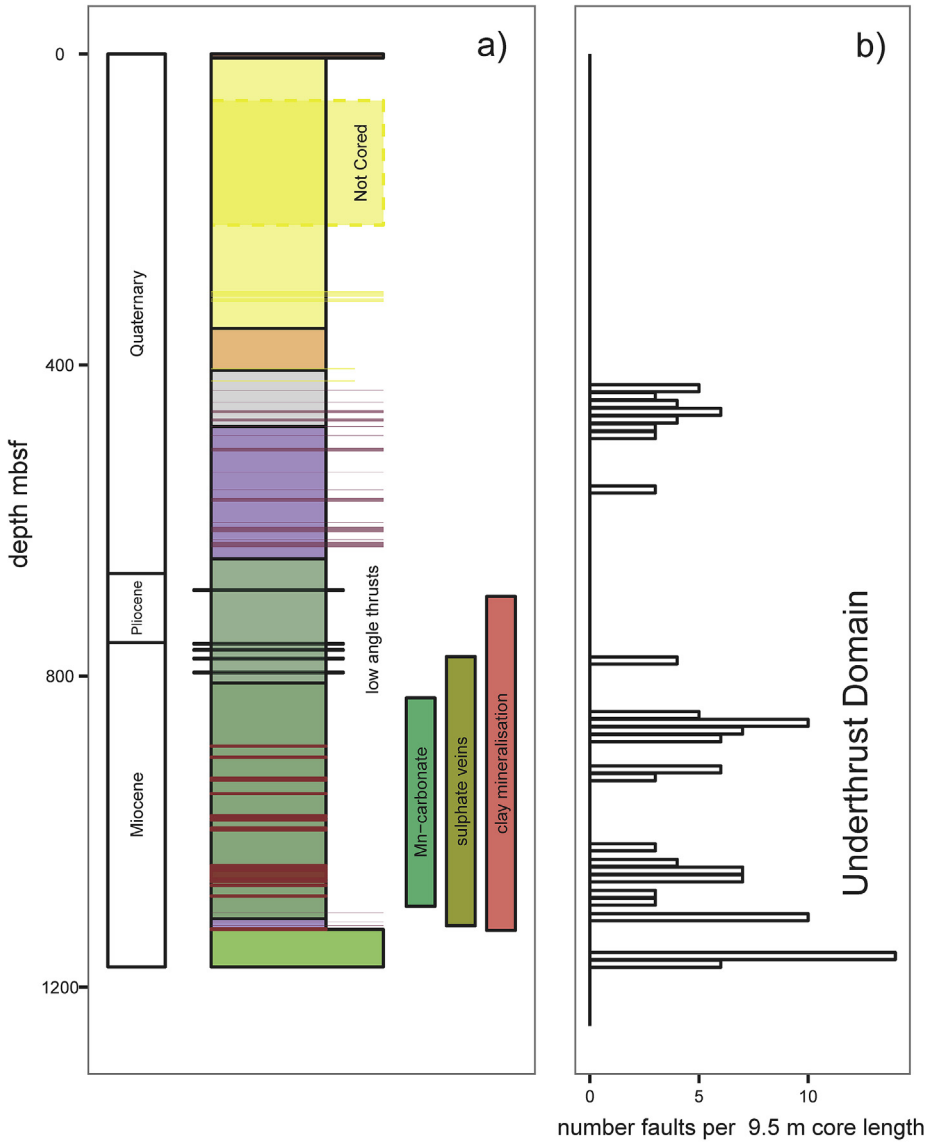

Fig. 2. a) Geological log illustrating general lithostratigraphic details of outer Nankai Accretionary Complex at Site C0023. Stratigraphic column; light green = basaltic basement; olive green = mudstones of the Lower Shikoku Basin formation, intervals with stratabound epigenetic mineralization are purple; grey, brown and pale yellow = hemiplegic mudstones of the Trench Wedge facies. The depth ranges of hydrothermal mineralization and are shown as are major thrusts within the décollement zone. b) Number of extensional faults and mineralized veins visible in hand specimen per 9.5 m interval (maximum core length), taken from Heuer et al., (2017). (For interpretation of the references to color in this figure legend, the reader is referred to the Web version of this article.)

C0023, they are limited to sediments overlying the basaltic basement, a feature seen in umbers from type localities from Cyprus (Pritchard and Maliotis, 1995). Their mode and habit of alteration is clearly different to the hydrothermal assemblages we present later.

Thermal maturation at sites near C0023 was previously modelled by Horsfield et al. (2006) using a basin modeling approach. In such an approach, many physical properties are made time-variant and during subsequent burial these properties approach present-day values. Time-variant properties within the simplest 1D basin models include porosity (Athy, 1930), thermal conductivity (Midttømme and Roaldset, 1999), fluid saturations, measures of diagenetic status (e.g. vitrinite reflectance, Sweeney and Burnham, 1990) and the thermal boundary conditions of the model. An important conclusion from previous basin modeling studies was that sites that are near to C0023, such as ODP Site 1174, while hot relative to typical sedimentary basins or ocean crust, must have been hotter in the past to account for the current diagenetic status of their sedimentary organic matter, and that the thermal conditions needed for petroleum generation are met in the deeper sections (Horsfield et al., 2006). More generally it is also known that in comparison to neighboring localities within the Nankai Trench, and also sedimentary basins more generally, present-day temperatures at the toe of the Nankai Accretionary Complex increase rapidly with respect to depth (Harris et al., 2013).

Hydrothermal activity and hot fluids can affect organic thermal maturity parameters in several ways. At a far-field scale, hot fluids may play a role in redistributing heat in active rifting environments, which may cause some areas of a basin to exhibit higher geothermal gradients than other areas (Parnell, 2010). However, in this situation thermal regimes caused by the flow of hot fluids do not differ markedly from those typically expected for burial diagenesis (Mackenzie et al., 1981; Nadeau, 2011). On the other hand, within a marine environment, hydrothermal activity has also been shown to alter the thermal maturity of organics at spreading centers (Simoneit and Lonsdale, 1982), and within hydrothermal systems hosted within impact craters (Parnell et al., 2007). In these cases hydrothermal systems operate at temperatures of 250–300 °C, with durations of around 10,000 years. However, there are many situations where hot fluids within sedimentary basins show no measurable effects on the thermal maturity of organic matter, even though there is incontrovertible evidence for hot fluids in the form of fission tracks, fluid inclusions or mineralization consistent with higher temperatures (Lampe et al., 2001; Parnell, 2010). In these instances hot fluids are considered to represent short term pulses, or short term events that may be at odds with both present day conditions, as well as those that typically prevailed during the past.

The aim of the current work is to elucidate the overall heating associated with hydrothermal mineralization and burial diagenesis within

underthrust sediments at Site C0023. The principle tools for doing this are (1) measurements of fluid inclusion homogenization temperatures and occurrences of mineralization, (2) biomarker derived measurements of thermal alteration of organic matter, and (3) models of thermal alteration within the vicinity of hydrothermal mineralization and thermal alteration due to burial (e.g., burial metamorphism of organic matter). In this approach thermal modeling is truthed against measurements of mineralization and biomarker thermal maturity parameters so that changes in temperature over geological time can be determined and the likely contribution of different heating processes evaluated.

2. Material and methods

2.1. Geological setting for C0023

Sediment cores were sampled during IODP Expedition 370 - Temperature Limit of the Deep Biosphere off Muroto. Site C0023 (32°22.00′N, 134°57.98′E) is located in the vicinity of ODP Sites 808 and 1174 at the protothrust zone in the Nankai Trough off Cape Muroto at a water depth of 4776 m (Fig. 1). These sites are located at the seaward end of the Muroto Transect, which is part of a series of NW to SE transects covering the off-shore geology of Southeastern Japan. Site C0023 is one of the most easterly in region, with only Site 1173 being further off-shore and eastward of the seafloor expression of the Nankai Trough (Heuer et al., 2017). During Expedition 370, aboard *D/V Chikyu*, cores were recovered at typically 3–9 m lengths between 189 and 1177 m below seafloor (mbsf), which was sectioned and subjected to x-ray computed tomography (XCT) imaging before visual description (Heuer et al., 2017; Tonai et al., 2019). Samples used for this study are listed in Tables 1 and 2.

In terms of general geological setting, the basaltic basement at site C0023 is overlain by sediments deposited from the Miocene to Quaternary (Hagino and the Expedition 370 Scientists, 2018), with the bottom section deposited in an ocean basin (Taira and Ashi, 1993). The site experienced sedimentation under trench conditions from the Pleistocene to the present day due to the subduction of the Philippine plate beneath the Pacific Plate, and in this relatively short period of time a further a further 600 m of sediment rapidly accumulated (Heuer et al., 2017). Site C0023 is at the seaward-end of the Nankai Accretionary prism, which has formed by the off-scrapping of sediment from the descending Philippine Plate (Pisani et al., 2005). Because of the location of site C0023 at the most distal end of the prism it is only minimally influenced by structural deformation, and this influence manifests as a proto-décollement zone comprising brecciated and intact intervals separated by low angle thrusts between 758 and 796 mbsf (Heuer et al., 2017).

Table 1
Fluid inclusion parameters.

	depth	Homogenization Temperature	Pressured Corrected Range	Melting point	Salinity Range
	mbsf	˚C	˚C	˚C	% NaCl equiv
C0023A-77R-2, 79–90 cm	821	98			
		100			
n = 2			118–141		
C0023A-86R-2, 0–10 cm	890	125			
		127			
n = 5		128			
		133			
		138			
			144–179		
C0023A-98R-1,0–5 cm	1010	128		−19	
		150		−12	
n = 5		159		−15	
		170		−21	
		148		−24	
			146–219		15–25
		+/- 5 ˚C		+/- 2 ˚C	

Table 2
Biomarker thermal maturity parameters.

Sample	depth	Sterane	Hopane	
	mbsf	% C_{29} 20 S	% C_{31} 22 S	% C_{30} ββ
C0023A-7X-5, 96.0–98.0 cm	311	41	53	42
C0023A-11F-1, 10.0–12.0 cm	355	40	44	29
C0023A-14X-CC, 8.0–10.0 cm	406	47	44	32
C0023A-16R-5, 22.0–24.0 cm	415	43	33	45
C0023A-20R-3, 64.0–66.0 cm	450	34	37	42
C0023A-23R-4, 40.0–42.0 cm	479	43	43	31
C0023A-24R-5R, 31.0–37.0 cm	489	43	46	49
C0023A-30R-3, 95.5–97.0 cm	539	38	41	42
C0023A-33R-5, 72.0–74.0 cm	565	46	36	52
C0023A-36R-5, 118.0–120.0 cm	589	41	40	46
C0023A-44R-8, 93.5–95.5 cm	666	39	44	46
C0023A-45R-2, 122.5–124.5 cm	671	27	38	44
C0023A-46R-2, 55.0–57.0 cm	675	43	32	56
C0023A-47R-2, 73.0–75.0 cm	680	38	34	59
C0023A-51R-3, 68.0–70.0 cm	701	13	24	56
C0023A-52R-2, 40.0–42.0 cm	704	25	40	43
C0023A-59R-4, 37.5–39.5 cm	740	17	33	53
C0023A-61R-2R, 36.0–37.5 cm	749	12	29	53
C0023A-62R-2, 79.0–82.0 cm	754	14	42	52
C0023A-63R-2, 112.0–114.5 cm	760	15	35	56
C0023A-64R-1, 128.5–130.5 cm	764	13	31	53
C0023A-66R-4, 12.0–14.0 cm	775	11	22	56
C0023A-72R-2R, 72.0–76.0 cm	799	11	20	52
C0023A-76R-1, 109.0–111.0 cm	817	23	25	49
C0023A-78R-2, 37.0–39.0 cm	825	26	44	35
C0023A-79R-3, 110.0–112.0 cm	832	16	53	24
C0023A-80R-4, 31.0–38.0 cm	837	–	36	43
C0023A-80R-4, 38.0–44.0 cm	837	26	32	41
C0023A-80R-5R, 15.0–20.0 cm	838	22	57	18
C0023A-81R-2, 60.0–64.0 cm	844	24	–	–
C0023A-81R-2, 64.0–69.0 cm	844	27	45	26
C0023A-81R-1, 78.0–81.0 cm	845	22	42	30
C0023A-81R-2, 69.0–74.0 cm	848	21	43	31
C0023A-82R-1, 23.0–32.0 cm	852	15	43	35
C0023A-82R-1, 68.5–70.5 cm	853	22	45	23
C0023A-83R-4, 93.0–95.0 cm	867	22	43	28
C0023A-86R-2R, 65.0–70.0 cm	892	19	41	32
C0023A-89R-2, 68.0–70.0 cm	920	21	42	26
C0023A-90R-1, 100.0–103.0 cm	929	17	38	27
C0023A-93R-2, 33.0–35.0 cm	958	25	34	25
C0023A-94R-4, 62.0–64.0 cm	972	25	38	21
C0023A-100R-6, 70.5–73.5 cm	1036	26	45	27
C0023A-102R-7, 84.5–87.0 cm	1058	29	64	11
C0023A-104R-3, 104.5–106.5 cm	1074	39	52	15
C0023A-106R-1, 88.0–90.0 cm	1091	47	58	12
C0023A-107R-1, 48.0–50.0 cm	1099	44	57	15
C0023A-108R-3, 50.0–52.0 cm	1111	38	61	14
C0023A-109R-2, 11.0–13.0 cm	1120	49	54	9
C0023A-110R-2, 10.0–12.0 cm	1122	43	59	9
C0023A-110R-2, 27.0–30.0 cm	1123	46	54	7
		+/- 5%	+/- 5%	+/- 3%

Thermal maturity parameters calculated using peak heights as follows. Using the 217 m/z ion chromatogram, Sterane C_{29} 20S = C_{29} 5α, 14 α,17α (H) 20S/(C_{29} 5α, 14 α,17α (H) 20S + C_{29} 5α, 14 α,17α (H) 20R). Using the 191 m/z ion chromatogram, Hopane % C_{31} 22 S = C_{31} 17 α, 21β (H) 22S/C_{31} 17 α, 21β (H) 22S + C_{31} 17α, 21β (H) 22R and Hopane % C_{30} ββ = C_{30} 17β, 21β (H)/(C_{30} 17β, 21β (H)+ C_{30} 17β, 21α (H)+ C_{30} 17α, 21β (H)).

2.2. Data sources

Geological description, including microscopy and scanning electron microscopy, downhole temperature data, porewater concentrations, x-ray fluorescence (XRF) elemental oxide abundances and scanning XCT data were taken from Heuer et al. (2017) and methods for their

Table 3
Time Temperature curves describing cooling in thermal aureole of vein.

	Zone I (821 mbsf)		Zone II (904 mbsf)		Zone III (1010 mbsf)	
	Vein contact	15 cm beneath contact	Vein contact	15 cm beneath contact	Vein contact	15 cm beneath contact
hrs	˚C	˚C	˚C	˚C	˚C	˚C
0.0	89.92	90.53	98.52	98.96	106.86	107.10
0.4	89.94	90.55	98.55	98.99	106.88	107.13
0.9	89.96	90.57	98.57	99.03	106.91	107.15
1.3	89.98	90.60	98.60	99.07	106.93	107.18
1.8	90.00	90.63	98.63	99.11	106.95	107.21
2.2	90.02	90.65	98.66	99.14	106.97	107.24
2.6	90.04	90.68	98.68	99.18	107.00	107.27
3.1	90.06	90.71	98.71	99.22	107.02	107.30
3.5	90.08	90.73	98.74	99.26	107.04	107.34
3.9	90.10	90.76	98.77	99.30	107.07	107.37
4.4	90.12	90.79	98.80	99.34	107.09	107.40
4.8	90.15	90.82	98.83	99.38	107.12	107.43
5.3	90.17	90.85	98.86	99.43	107.14	107.47
5.7	90.19	90.88	98.89	99.47	107.16	107.50
6.1	90.22	90.91	98.92	99.51	107.19	107.54
6.6	90.24	90.95	98.95	99.55	107.22	107.57
7.0	90.26	90.98	98.98	99.60	107.24	107.61
7.4	90.29	91.01	99.01	99.64	107.27	107.64
7.9	90.31	91.05	99.04	99.69	107.29	107.68
8.3	90.34	91.08	99.07	99.74	107.32	107.72
8.8	90.36	91.12	99.11	99.78	107.35	107.76
9.2	90.39	91.15	99.14	99.83	107.38	107.79
9.6	90.41	91.19	99.17	99.88	107.40	107.83
10.1	90.44	91.23	99.21	99.93	107.43	107.87
10.5	90.47	91.27	99.24	99.98	107.46	107.92
11.0	90.50	91.31	99.27	100.03	107.49	107.96
11.4	90.52	91.35	99.31	100.08	107.52	108.00
11.8	90.55	91.39	99.34	100.13	107.55	108.04
12.3	90.58	91.43	99.38	100.18	107.58	108.09
12.7	90.61	91.47	99.42	100.24	107.61	108.13
13.1	90.64	91.52	99.45	100.29	107.64	108.17
13.6	90.67	91.56	99.49	100.35	107.67	108.22
14.0	90.70	91.61	99.53	100.40	107.70	108.27
14.5	90.74	91.65	99.57	100.46	107.73	108.31
14.9	90.77	91.70	99.61	100.52	107.76	108.36
15.3	90.80	91.75	99.65	100.58	107.80	108.41
15.8	90.83	91.80	99.69	100.64	107.83	108.46
16.2	90.87	91.85	99.73	100.70	107.86	108.51
16.6	90.90	91.90	99.77	100.76	107.90	108.56
17.1	90.94	91.96	99.81	100.82	107.93	108.62
17.5	90.98	92.01	99.86	100.89	107.97	108.67
18.0	91.01	92.07	99.90	100.95	108.00	108.73
18.4	91.05	92.13	99.95	101.02	108.04	108.78
18.8	91.09	92.19	99.99	101.09	108.08	108.84
19.3	91.13	92.25	100.04	101.16	108.12	108.90
19.7	91.17	92.31	100.09	101.23	108.15	108.95
20.1	91.21	92.37	100.13	101.30	108.19	109.01
20.6	91.26	92.44	100.18	101.37	108.23	109.07
21.0	91.30	92.50	100.24	101.44	108.27	109.14
21.5	91.35	92.57	100.29	101.52	108.31	109.20
21.9	91.39	92.64	100.34	101.60	108.36	109.26
22.3	91.44	92.71	100.40	101.68	108.40	109.33
22.8	91.49	92.79	100.45	101.76	108.44	109.40
23.2	91.54	92.86	100.51	101.84	108.49	109.47
23.7	91.59	92.94	100.57	101.92	108.53	109.54
24.1	91.64	93.02	100.63	102.01	108.58	109.61
24.5	91.70	93.10	100.69	102.10	108.63	109.68
25.0	91.75	93.18	100.76	102.19	108.68	109.75
25.4	91.81	93.27	100.83	102.28	108.73	109.83
25.8	91.87	93.35	100.90	102.38	108.78	109.91
26.3	91.94	93.44	100.97	102.47	108.83	109.98
26.7	92.00	93.54	101.04	102.57	108.89	110.06
27.2	92.07	93.63	101.12	102.67	108.94	110.15
27.6	92.14	93.73	101.20	102.78	109.00	110.23
28.0	92.21	93.83	101.28	102.88	109.06	110.32
28.5	92.29	93.94	101.37	102.99	109.13	110.40
28.9	92.36	94.04	101.46	103.10	109.19	110.49
29.3	92.45	94.15	101.55	103.22	109.26	110.59
29.8	92.53	94.27	101.65	103.34	109.33	110.68
30.2	92.62	94.38	101.76	103.46	109.41	110.78
30.7	92.72	94.50	101.86	103.58	109.48	110.88
31.1	92.82	94.63	101.98	103.71	109.56	110.98
31.5	92.92	94.75	102.10	103.84	109.65	111.09
32.0	93.03	94.89	102.22	103.98	109.74	111.19
32.4	93.15	95.02	102.35	104.12	109.83	111.31
32.9	93.27	95.17	102.49	104.27	109.93	111.42
33.3	93.40	95.31	102.64	104.41	110.04	111.54
33.7	93.54	95.47	102.80	104.57	110.15	111.66
34.2	93.69	95.63	102.97	104.73	110.27	111.79
34.6	93.85	95.79	103.15	104.89	110.40	111.92
35.0	94.02	95.96	103.34	105.06	110.54	112.06
35.5	94.21	96.14	103.55	105.24	110.69	112.21
35.9	94.41	96.33	103.78	105.42	110.85	112.36
36.4	94.63	96.53	104.02	105.61	111.02	112.51
36.8	94.86	96.73	104.28	105.81	111.21	112.68
37.2	95.12	96.95	104.57	106.02	111.42	112.85
37.7	95.40	97.18	104.89	106.23	111.65	113.03
38.1	95.72	97.42	105.24	106.45	111.90	113.22
38.5	96.06	97.68	105.62	106.68	112.18	113.42
39.0	96.45	97.95	106.06	106.92	112.49	113.64
39.4	96.89	98.25	106.55	107.17	112.84	113.87
39.9	97.39	98.56	107.11	107.43	113.25	114.12
40.3	97.97	98.90	107.76	107.70	113.71	114.38
40.7	98.64	99.27	108.52	107.98	114.25	114.67
41.2	99.44	99.67	109.44	108.27	114.89	114.98
41.6	100.41	100.11	110.57	108.55	115.67	115.32
42.0	101.63	100.58	112.00	108.81	116.66	115.68
42.5	103.22	101.09	113.90	109.02	117.95	116.05
42.9	105.44	101.60	116.53	109.11	119.74	116.43
43.4	108.79	102.03	120.48	108.90	122.45	116.71
43.8	114.52	102.06	127.05	107.90	127.09	116.64
44.2	126.82	100.21	139.82	104.62	137.00	115.00
44.7	170.00	90.82	170.00	94.01	170.00	103.93
45.1	91.00	91.00	98.00	98.00	103.00	103.00

acquisition are reported therein. The homogenization temperatures of aqueous fluid inclusions were measured at the University of Aberdeen using a THMS-600 heating–freezing stage mounted on a Nikon Labophot transmission light microscope. The instrument is equipped with a range of objective lenses including a 100 × lens which was used for this work and was calibrated against synthetic H_2O (374.1 and 0.0 ˚C) and CO_2 (−56.6 ˚C) standards (Synthetic Fluid Inclusion Reference Set, Bubbles Inc., USA). The homogenization of aqueous two-phase inclusions was taken to indicate the temperatures at which the host mineral phase precipitated. Considering the possible range of pressures under which the inclusions were formed (between the seafloor and the present depth) and the observed salinity, we use the SoWat NaCl-H_2O package (Driesner and Heinrich, 2007; Driesner, 2007) to calculate the pressure-corrected ranges of trapping temperatures. Data are reported in Table 1.

2.3. GC-MS analysis of biomarkers

Samples were solvent extracted using Soxhlet apparatus (5–25 g of sediment or rock was extracted in dichloromethane/methanol 93:7 v/v for 48 h). The extract was fractionated using flash mini-column chromatography (silica column; hexane for saturated fraction; 3:1 v/v hexane/dichloromethane for aromatics fraction; 2:1 v/v dichloromethane/methane for polar fraction). The resulting saturate fraction was analyzed by gas chromatography-mass spectrometry (GC-MS). GC-MS was performed using a 6890N Network GC system interfaced to a 5975 inert mass selective detector. A PTV in injector (300 ˚C)

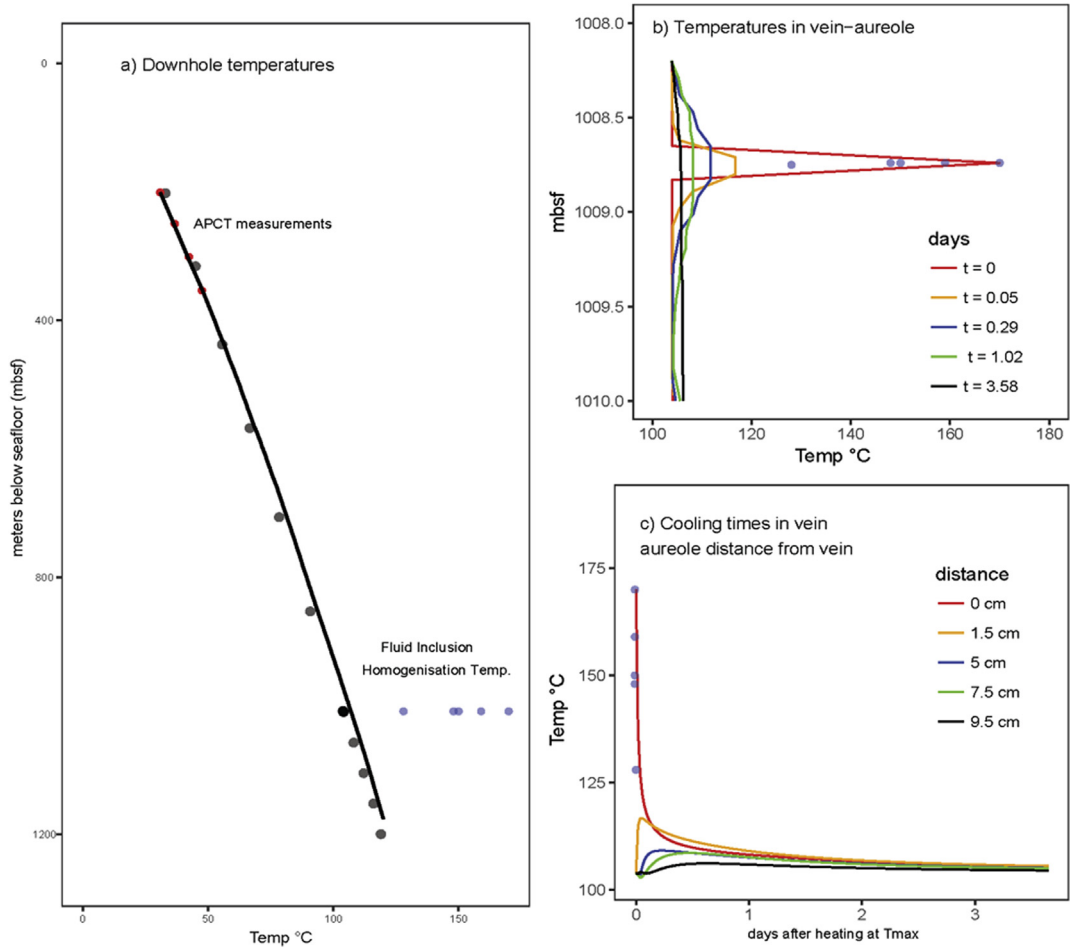

Fig. 3. Thermal modeling of the vein aureoles. a) Downhole temperatures red dots = downhole measurements, blue dots = fluid inclusion homogenization temperatures measured on aqueous inclusions in vein barite. b) Cooling around vein (days after heating) at 1010 mbsf heated to 180 °C. c) Cooling duration at set distance from vein at 1010 mbsf (days after heating). (For interpretation of the references to color in this figure legend, the reader is referred to the Web version of this article.)

operating in splitless mode was used and the GC temperature program was as follows; 60 °C–120 °C at 20 °C/min then from 120 °C to 290 °C at 4 °C/min. The column was Greyhound GC-5 (an HP-5 equivalent phase; 30 m length, 250 μm ID and 0.25 μm film thickness). The MS was operated in selected ion monitoring mode (less than 30 ions with a dwell time of less than 40 ms, ions included the *m/z* ions 85, 113, 183, 189, 191, 205, 217, 218, 259). Compounds were identified by reference to well-characterized samples of bitumen of analogous thermal maturity (sample of brown coal and a laboratory sample of North Sea Oil). Biomarker thermal maturity parameters are noted in the text and are expressed as a percentage (a number from 0 to 100). Inputs for biomarker thermal maturity parameters were measured using peak areas of compounds on the *m/z* 191 ion chromatogram for hopanes and *m/z* 217 ion chromatogram for steranes (measurements made using MSD-Chemstation).

Ion chromatograms illustrating pre-oil window and oil window biomarkers are shown in Supplementary Information 1. Samples that are pre-oil window but beginning to evidence thermal alteration (e.g., depths 700 to about 950 mbsf) generally have far higher proportions of the thermally immature C_{30} 17,21 ββ (H) hopane, and the C_{31} 17,21 ββ (H) 22R hopane (Farrimond et al., 1998). Samples that are in the oil window (about 1000 mbsf) have higher proportions of the 5α,14α,17α(H) 20(S) sterane isomer. These compounds were used to calculate the thermal maturity parameters described later. Data for biomarker thermal maturity parameters are presented in Table 2.

2.4. Thermal modeling of thermal aureoles around veins

Thermal modeling of alteration aureoles around veins was performed using Thermic, a finite element heat flow-modeling program (Bonneville and Capolsini, 1999). Models comprised a grid with a ~100 m spacing and localized refinement around regions of hydrothermal alteration. To establish the background heat flow regime, models were run to recreate present heat flow distributions obtained for Site C0023 during Expedition 370 (Heuer et al., 2017). To simulate the effects of temporary heating within mineralized regions of interest, a single line of nodes was instantaneously set to temperatures observed within fluid inclusions. Heat from this zone was allowed to dissipate and warm the neighboring region within the model. Particular attention was paid to the period of time at which temperatures were maintained at a level that permitted mineralization. Heating durations even a few days longer predicted far larger aureoles than those observed in the cores of Site C0023. The effect of this short-lived heating and cooling on surrounding sediments was evaluated at three depths within underthrust sediments. Time and temperature curves representative of cooling at different depths are presented in Table 3 and an example is plotted in Fig. 3b and c.

2.5. Basin modeling

Basin modeling was performed using the commercially available basin modeling package Petromod 2017. A 1D model was constructed

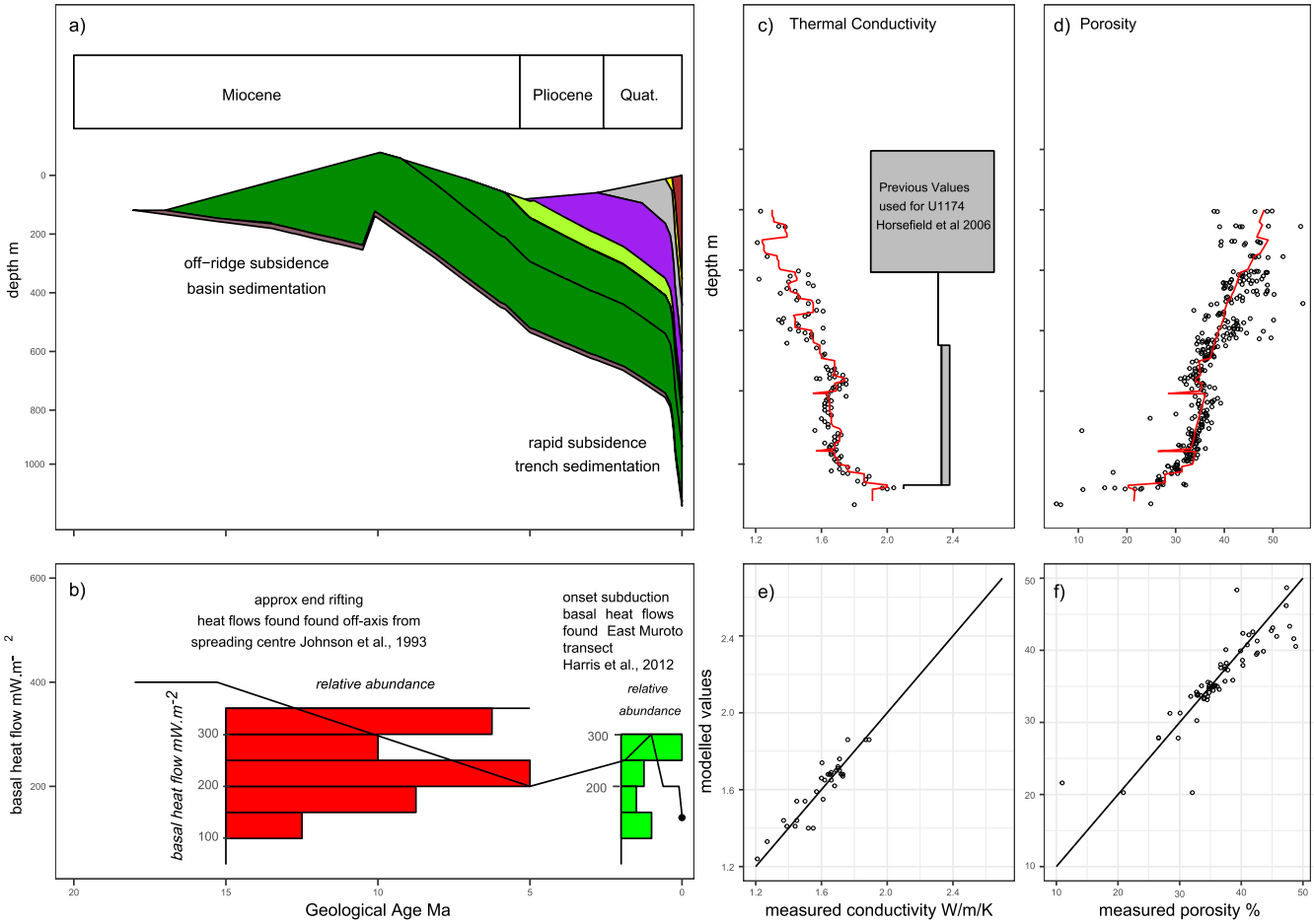

Fig. 4. Decompacted burial curve for Site C0023. b) Transition of Site C0023 through different heatflow environments over geological time, ending with present-day heatflow. Histograms show the relative abundance of basal heatflow for the off-axis region of a spreading center (red) and the Moroto transect (green). c) and d) Measured values of thermal conductivity and porosity taken from Heuer et al. (2017, black circles) and their values modelled from lithological mixtures inbuilt within Petromod, 2017 (red lines). The grey boxes show previous modelled conductivity used in Horsfield et al. (2006). e) and f) are cross plots illustrating goodness of fit between modelled and measured parameters (black lines are 1:1). (For interpretation of the references to color in this figure legend, the reader is referred to the Web version of this article.)

using lithological and biostratigraphic information from Heuer et al. (2017) and Hagino and the Expedition 370 Scientists, 2018. The decompacted burial curve for Site C0023 is shown in Fig. 4a. The model was populated with physical properties calculated for three-end-member mixtures of mud, volcaniclastic fragments and sand using the library inbuilt within Petromod. The models of porosity and thermal conductivity and their goodness of fit to measured data are shown within Fig. 4b. The fit of the lithology-modelled physical properties and those measured in the laboratory is mostly good (capturing features such as the thermal blanketing effect of overlying sediment), but the thermal conductivities both measured (real) and modelled are lower than those used in previous studies for nearby Site 1174 (Horsfield et al., 2006). The lithological data used to model physical properties were taken from Heuer et al. (2017) and derived from core description and smear slide petrography. Age data was taken from Hagino and the Expedition 370 Scientists (2018) with the base of the Pleistocene between 639.982 and 630.44 mbsf, and the base of the Pliocene between 796.53 and 769.44 mbsf.

A range of heat flow models was evaluated but only models in which past heat flows were higher than at the present day could match both biomarker thermal maturity parameters and present day temperature values, without physical properties of the model being altered (both petrophysical and geological). In this way our work is consistent with that of others (Horsfield et al., 2006); and shows that Site C0023, like Site 1174, is cooling at the present time. Much work has been undertaken in the region and many different palaeoheatflow cases could be justified (heat flow regimes both hotter and cooler than the present day), but we choose to derive paleoheatflow from well-cited accounts of the tectonic evolution of southeast Japan present in peer-reviewed literature (Mahony et al., 2011); in short, Site C0023 has experienced a transition from ridge-centered volcanic activity at a spreading center to regionally prevalent magmatism and the present-day subduction zone where hot fluids may circulate within the basement. Spreading processes within the Shikoku Basin started at 26 Ma and stopped around 15 Ma (Okino and Kato, 1995), and indicate the heat flow would therefore be high before 15 Ma but decrease rapidly after 15 Ma. This was embedded within the model by letting Site C0023 transition through a cooler range of off-axis heat flows measured at spreading centers at the present day (Johnson et al., 1993 – insert in Fig. 4b). Note that Site C0023 is subducted hot, before it cools to one of the lowest heatflows found at inactive spreading centers, and also that the highest temperatures associated with volcanic magmatism are not included in the model (these temperatures would not interact with the basin-fill). From 2 Ma to present, the number of polygenetic volcanoes along Kyushu notably increased, at least relative to periods of time before 2 Ma (Mahony et al., 2011). Within our model this relatively far-field aspect is represented by a brief increase in past heat flow around 2 Ma (in both our work and that of Horsfield et al., 2006 this is important for

Table 4
Temperature time curves from basin modeling.

Zone I (850 mbsf)		Zone II (950 mbsf)		Zone III (1075 mbsf)	
Age	Temperature	Age	Temperature	Age	Temperature
Ma	˚C	Ma	˚C	Ma	˚C
0	97	0	108	0	119
0.01	98	0.01	109	0.01	121
0.04	108	0.04	120	0.04	134
0.08	116	0.08	130	0.08	146
0.1	118	0.1	133	0.1	151
0.11	118	0.11	134	0.11	152
0.15	117	0.15	134	0.15	153
0.19	114	0.19	131	0.19	151
0.23	109	0.23	127	0.23	148
0.27	103	0.27	122	0.27	144
0.33	97	0.33	118	0.33	142
0.39	96	0.39	118	0.39	143
0.47	96	0.47	119	0.47	146
0.54	92	0.54	116	0.54	142
0.55	92	0.55	116	0.55	142
0.62	90	0.62	115	0.62	141
0.78	88	0.78	113	0.78	140
1.01	85	1.01	110	1.01	138
1.32	78	1.32	104	1.32	132
1.88	65	1.88	92	1.88	121
1.94	64	1.94	91	1.94	120
2.79	53	2.79	81	2.79	112
3	50	3	79	3	110
3.76	40	3.76	70	3.76	103
3.8	39	3.8	70	3.8	103
4.86	24	4.86	58	4.86	93
5	22	5	56	5	92
5.18	20	5.18	54	5.18	90
5.81	9	5.81	44	5.81	81
5.97	9	5.97	43	5.97	80
7.13	2	7.13	31	7.13	69
		7.83	23	7.83	61
		8.1	20	8.1	59
		8.53	15	8.53	54
		9.24	6	9.24	46
		9.94	2	9.94	39
				10.1	37
				10.5	33
				10.65	31
				11.32	23
				11.35	23
				12.06	14
				12.76	6
				12.8	6
				13.47	2

matching thermal maturity observations). At present, the heat flow in Hole C0023A is 140 mW m^{-2}, based on shipboard results (Heuer et al., 2017). Thus from 2 Ma to the present day, Site C0023 cools and transitions through the range of heat flows known from the eastward side of the Muroto transect (Harris et al., 2013). While it is the case that biomarker-calibration data could only be matched by models in which heat flow at Site C0023 declined from 2 Ma, formations in underthrust sediments have only recently begun to cool from about 0.1 Ma. Thus despite a recent cooling, heat flow at Site C0023 is nonetheless high relative to typical sedimentary basins (MacKenzie and Craw, 1993; Nadeau et al., 2011).

Aside from basal heat flow, the other major boundary condition which can be time variant is the sediment-water interface temperature (SWIT). Along with present day measurements of downhole temperature, past sediment water interface temperature forms a crucial boundary condition that the model recreates (at each timestep in the case of SWIT). Past SWITs were set to a constant value of 2 ˚C (present day temperature) to avoid having multiple variant boundary conditions, for a parameter which has likely varied little (the site has been in deepwater environment since basement formation). Burial curves indicative of thermal regimes within the underthrust sediments are presented in Table 4.

3. Results

3.1. Disposition, petrography and heat-flow models of hydrothermal mineralization

A distinctive difference between the characterizations of Sites 1174 (Underwood et al., 1993) and C0023 was the recognition of hydrothermal mineralization between 775 and 1121 mbsf at Site C0023. The mineralization has two elements: veins and stratabound patches of pale-yellow alteration 10–50 cm thick. The patches of stratabound alteration do not pervade the entire interval, but instead are interspersed as distinct packages within host-sediment (Fig. 5a). At its most intense, patches of pale-yellow alteration cluster around burrows and fade laterally with distance from a center or core in which coloration is all-pervasive. Such mineralization is not found in burrows in overlying sediments (contrast Fig. 6a and b to 6c). The pale-yellow patches correspond to increases in density measurable by XCT (see Tonai et al., 2019 for further description). This disposition contrasts to that of the umber at the base of the site where reddening is more uniform and bedding parallel (Heuer et al., 2017).

Different zones of mineralization are shown in Fig. 6 and these represent an increasing prevalence with depth, although it needs to be noted that mineralized intervals are never all-pervasive and that unaltered lithologies always dominate. In the shallowest Zone I (Fig. 6), vein mineralization is present, and there is less deformation of veins and no stratabound alteration patches. In Zone II, stratabound mineralization is observed in addition to barite veins, but it is of low prevalence. In Zone III, vein and stratabound mineralization is typically more pervasive and trapping temperatures of fluid inclusions exceed that needed for the precipitation of barite under the condition of retrograde solubility.

The vein mineralization consists of crystalline barite and minor anhydride. It occupies extensional faults within the underthrust domain (Figs. 2 and 7) and is not present in the basaltic basement or overlying prism sediments. The extensional faults hosting barite veins may have developed early in the Shikoku Basin sediments, during their accumulation in a back-arc rift (Hibbard et al., 1993), and/or developed subsequently or been reactivated as sediments shear parallel to the direction of the subducting plate (Bangs et al., 2009). The veins have varied morphologies and are present as both void-filling euhedral crystals (e.g., 832 mbsf) indicating growth within open spaces (suggesting that faulting has not yet affected newly formed mineralization, Fig. 7a) and also as slicken-crysts (e.g., 931 mbsf, Fig. 7b) indicating deformation of veins within active fault planes. In some cases, the veins are multi-generational (Fig. 7c) and one phase of mineralization is discordant within the shear fabric developed in another, indicative of multiple phases of fracture-opening and mineralization (Bons et al., 2012). Thus some of the mineralization has not been affected by recent deformation phases, implying a relatively recent origin, or that some at least post-dates the extensional straining of sedimentary fabrics.

Stratabound mineralization when most intense overprints the entirety of the original sedimentary fabric, whilst at the margins or where less intense it can be seen to preferentially follow burrows and related ichnofabrics (Fig. 5a and b). Rhodochrosite-rich patches are often yellow, but notably pink when mineralization is less pervasive (Fig. 5b). Euhedral Barite within burrows can be seen to have intergrown with rhodochrosite, calcite and smectite (Fig. 8a) Replacement of diatoms and other bioclasts by rhodochrosite and barite is common (Fig. 8a) and where replacive mineralization is sufficiently pervasive, the detailed morphology of pre-existing clasts is not seen (Fig. 8b).

Euhedral barite in underthrust sediments reveals the low-temperature hydrothermal nature of the mineralization. The barite contains two-phase aqueous inclusions with homogenization temperatures

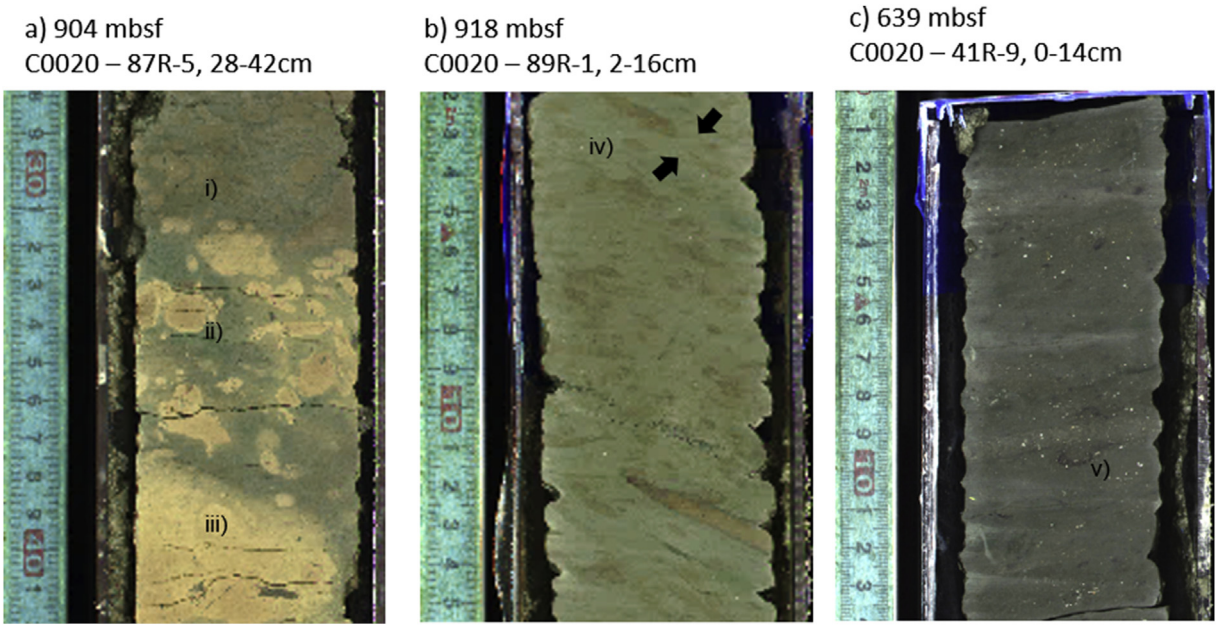

Fig. 5. Stratabound mineralization. a) Less intense i) and intense ii) stratabound mineralization in Lower Shikoku Basin formation (core 87R-5) ~904 mbsf, Mn-carbonate mineralization (pale brown and pale yellow) follows burrows. iii) Rhodochrosite mineralization only. b) Stratabound mineralized burrows (e.g., iv) strained so that burrows are compacted (see arrows) relative vertical dimension and elongated relative to horizontal dimension (core 89R-1, 919 mbsf). c) Unaltered burrows (e.g., v) from the overlying accretionary complex. (For interpretation of the references to color in this figure legend, the reader is referred to the Web version of this article.)

ranging from 98 to 100 °C at 822 mbsf to 128–175 °C at 1010 mbsf (+/-5 °C). Larger fragments of vein-barite recovered at 1010 mbsf (Fig. 7d) yielded melting temperatures of −19 to −24 °C, indicating salinities of 16–25% NaCl equivalent (Table 1). This range of homogenization temperatures and salinities is typical of hydrothermal mineralization formed from the mixing of deeper, more-saline fluids (> 5% NaCl equivalent), and less-saline interstitial water (e.g., the Irish type and the "epithermal" type fields in Wilkinson, 2001). The ranges are distinctively different from the present-day temperature and salinity at Site C0023 for all the depths where fluid inclusions have been measured (present day temperatures are less than 120 °C and interstitial water has 3 % wt equiv. NaCl, Heuer et al., 2017).

Considering the salinity ranges measured for the fluid inclusions, and allowing for the formation of the barite at depths from ~4776 m subsea to present-day subsurface depths (5956 m subsea), likely trapping temperatures can be calculated for the fluids. These data are shown in Table 1, where the lower bound of trapping temperatures represents trapping at the seafloor whilst the upper bound trapping at overburden pressures equating to the current depth of the barite. Fluid inclusions in the barite at 822 mbsf were trapped at 118–141 °C, whilst at 1010 mbsf temperatures were 146–219 °C.

Heat-flow models were used to evaluate the size of the thermal aureoles created by the incursion of hot fluids into faults and permeable sedimentary fabrics such as burrows, and the capacity of this heating to produce mineralization. In our models, heating occurs as time-limited events, in which a small region is heated to 180 °C (the highest homogenization temperature from fluid inclusions) and then allowed to cool. The models showed that further than 30 cm away from the vein or alteration patches, temperatures would not be greatly elevated above background levels (Fig. 3b and c).

Such thermal alteration is relatively mild, but sufficient to change the solubility of the sulfate and carbonate minerals observed (i.e. the tendency for certain minerals to be less soluble at higher temperatures – this temperature is plotted for barite in Fig. 6a; Blount, 1977; Plummer and Busenberg, 1982; Wolfram and Krupp, 1996). Under hydrostatic pressures within the underthrust sediments, and for the concentration of barium dissolved within porewaters (< 120 μM from Heuer et al., 2017), retrograde solubility for barite would occur above 145 °C and would vary only slightly with pressure for the range of hydrostatic pressures under consideration (Blount, 1977). Similar solubility behavior can be assumed for carbonate mineralization (Plummer and Busenberg, 1982). Temperature curves representative of cooling at different depths are presented in Table 3. We note also that the deepest zone of mineralization (Zone III), exhibits fluid inclusion temperatures that can exceed that needed for retrograde solubility by the greatest amount (Fig. 6a) and that here dissolved inorganic carbon concentrations are lowest and carbonate concentrations greatest (Fig. 6c and d).

3.2. Biomarker measures of thermal maturity

Thermal maturation was gauged by using three biomarker thermal maturity parameters calculated from hopane and sterane biomarkers. The benefit of using three thermal maturity parameters is that they can be cross-compared for consistency. This is done in Figs. 9 and 10. All three parameters indicate exposure to thermal regimes in which catagenesis has begun, but prolific petroleum generation is mostly absent; e.g. a thermal state in which the generation of hydrocarbons is not yet prolific or at a commercial rate but where organic compounds such as biomarkers are being released from kerogen (VRE ~ 0.65–0.70% - taken from Killops and Killops, 2005). The hopane % ββ parameter captures the declining proportion of 17,21 ββ (H) hopane. This decline occurs because 17,21 ββ (H) hopane is thermally broken-down at the onset of petroleum generation (% ββ < 0.1) and because other, more thermally stable, hopane isomers are generated from kerogen decreasing its relative proportion (the onset for this is at % ββ < 0.4 - Farrimond et al., 1998). Values for the % ββ parameter less than 10% are found only at the base of the hole, whereas values of 40% are found beneath 890 mbsf and at some regions from 820 to 870 mbsf (Figs. 9 and 10).

At Site C0023 the sterane % 20S parameter closely mirrors the % ββ hopane parameter. Unlike the 17,21 ββ (H) hopane, the 5,14,17 ααα(H) sterane isomers have thermal stabilities that help them persist further into the oil window. Values of the 20S parameter greater than 40% are associated with petroleum generation, whereas values less

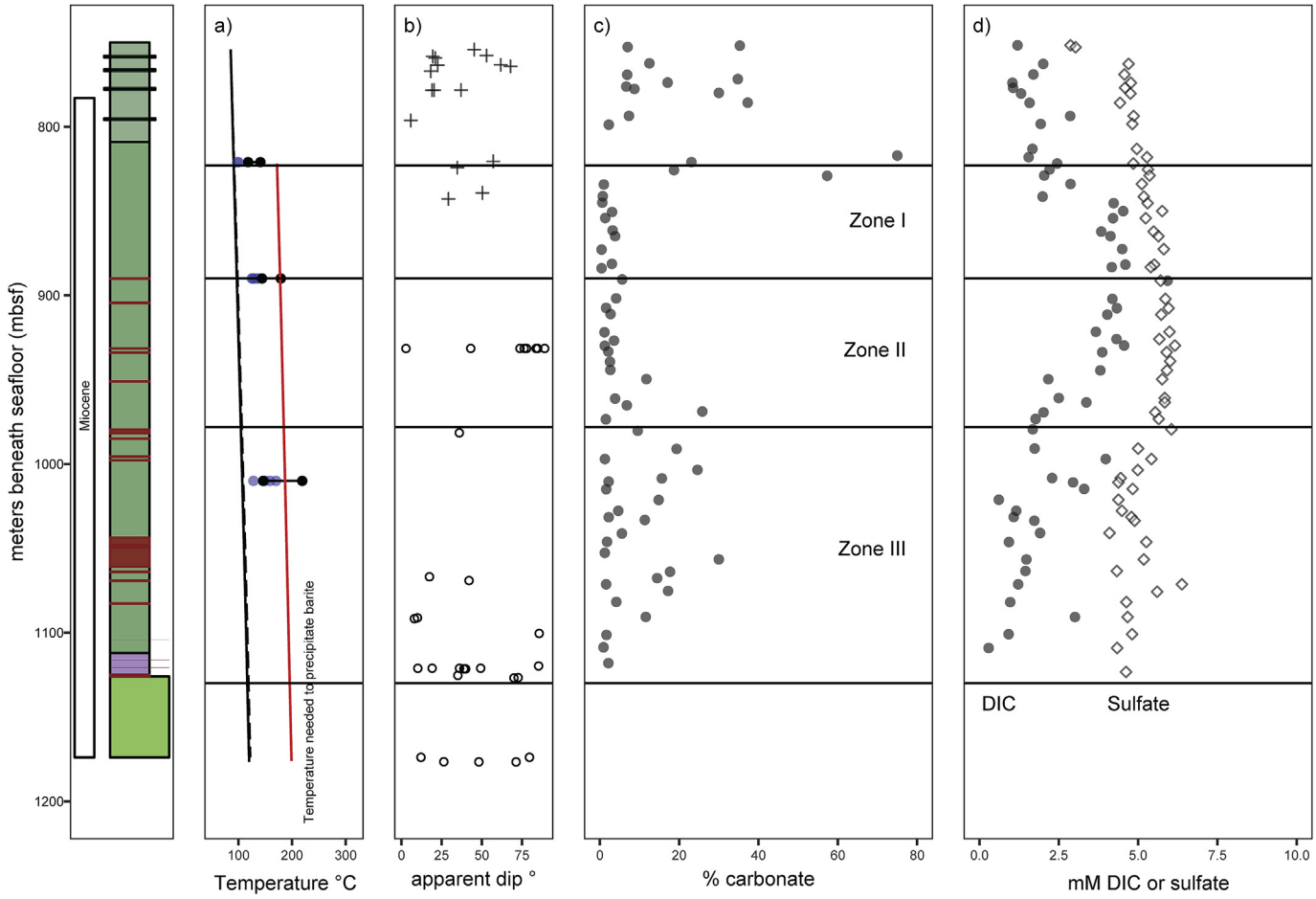

Fig. 6. Downhole plot of the effects of mineralization and mineralization zones. a) Blue dots = measured fluid inclusion homogenization temperatures; black dumbbells = pressure corrected maximum and minimum trapping temperatures; black line = present day temperature; red-line = temperature above which retrograde solubility of barite occurs. b) cross = measured inclination of thrust surfaces; open circle = measured inclination of extensional fault surfaces. c) % carbonate by weight in sediments. d) shade circle = dissolved inorganic carbon (DIC); open circle = dissolved sulfate in porewater. (For interpretation of the references to color in this figure legend, the reader is referred to the Web version of this article.)

than 40% but greater than 20% are associated with mild levels of catagenesis and the generation of the 5,14,17 ααα(H) 20 S isomer from kerogen (Farrimond et al., 1998). Thus beneath ~1075 mbsf, where the sterane parameter exceeds 40% rates of petroleum generation could be significant.

The % 22 S hopane parameter is also shown (Figs. 9 and 11). It shares similarities with both the % 20S sterane parameter and the % ββ hopane parameter; high values at the base and some higher values from 800 to ~850 mbsf. The main difference between the % ββ hopane and %20S parameter and the % 22 S hopane parameter is between 850 and 950 mbsf, where its values are as high as 55% (indicating a high thermal maturity), but the other parameters indicate much lower thermal maturities. An aspect of the organic matter that was noted by Horsfield et al. (2006) was the high proportion of reworked organic matter (organic matter that has already been thermally matured in another setting prior to its deposition). Sedimentary organic matter in subsea volcanic sediments can acquire a thermal history sufficient to form petroleum biomarkers (Bowden et al., 2016), and as hopanes are more chemically resistant than steranes in surface environments (Watson et al., 2002) and more thermally resistant than ββ hopanes (Farrimond et al., 1998), reworked and resedimented thermally mature organic matter would contain higher proportions of 22S hopanes. Thus while all the three biomarker parameters are mostly consistent in portraying similar levels of thermal alteration at most depths, for the narrow depth range between 900 and 950 the high values observed solely for the 22S hopane-parameter are likely due to reworked organic matter that has already experienced a thermal history.

4. Discussion

4.1. Paragenesis and the passage of hot fluids

A paragenetic sequence of events for Site C0023 is summarized in Fig. 11a. Mineralization within sediments immediately overlying the basaltic crust comprises heamatized sediments and limited deposition of calcite veins (Fig. 11b and c). Both reddening and calcite veins are also found in underlying basalts to a limited degree; veins are mostly on the surfaces of pillows and where red clays are present within the basalt they coat inter-pillow voids (e.g., the surfaces of pillows). The close spatial association of reddening and basalts, low-temperature mineral assemblages such as calcite, and vein systems that penetrate both crust and sediment are features described from umbers (Robertston, 1975; Pritchard and Maliotis, 1995). This mineralization style is not found in the overlying intervals above 1124 mbsf at Site C0023 (sediments in this region are not in contact with basalt).

The relative timing of barite, anhydride and rhodochrosite mineralization 775 to 1121 mbsf within burrows can be obtained by comparing the presence or absence of deformation features. For stratabound mineralization it is notable that some of the mineralized burrows within hydrothermal aureoles are strained relative to their counterparts above the décollement zone (compare Fig. 5a – oblate burrows and 6b sheared burrows). Therefore some of the mineralized burrows are

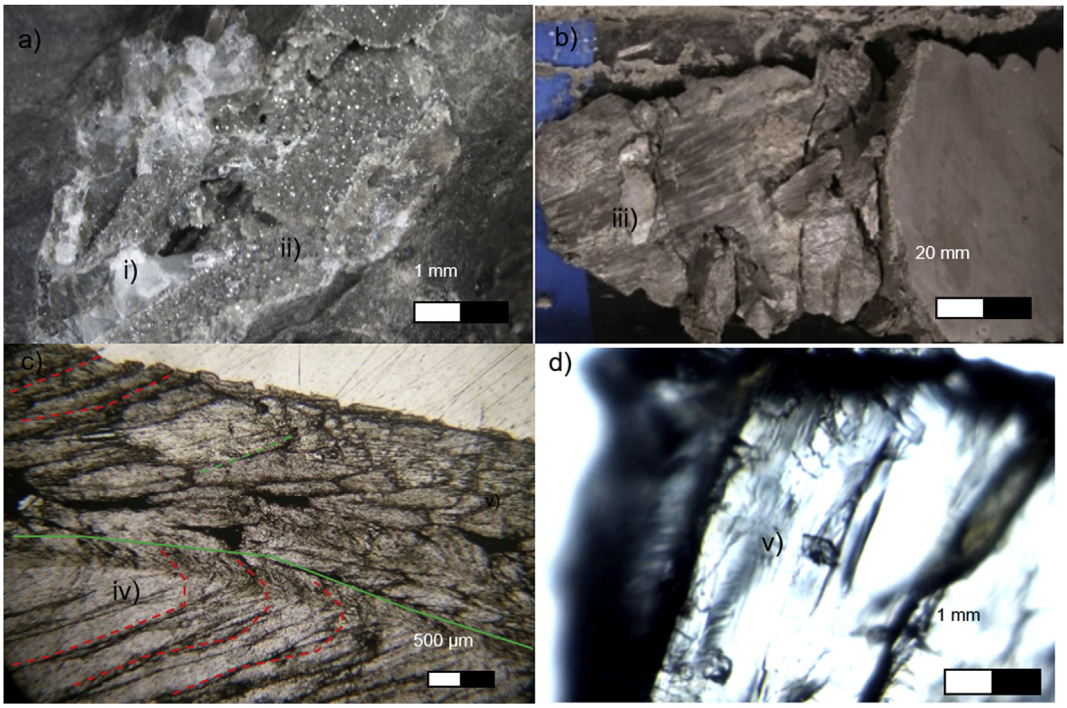

Fig. 7. Barite in underthrust sediments. a) Euhedral blocky barite i) and ii) botryoidal barite within open fracture 821 mbsf; b) Barite slickencrysts iii) on a slickened surface at 931 mbsf; c) Vein barite with comb-texture from 1010 mbsf. Fibrous crystals evidence shearing iv) are terminated by later growth of barite with new orientation and inclusions of bitumen and pyrite v); d) two-phase aqueous inclusions within vein-barite from 1010 mbsf.

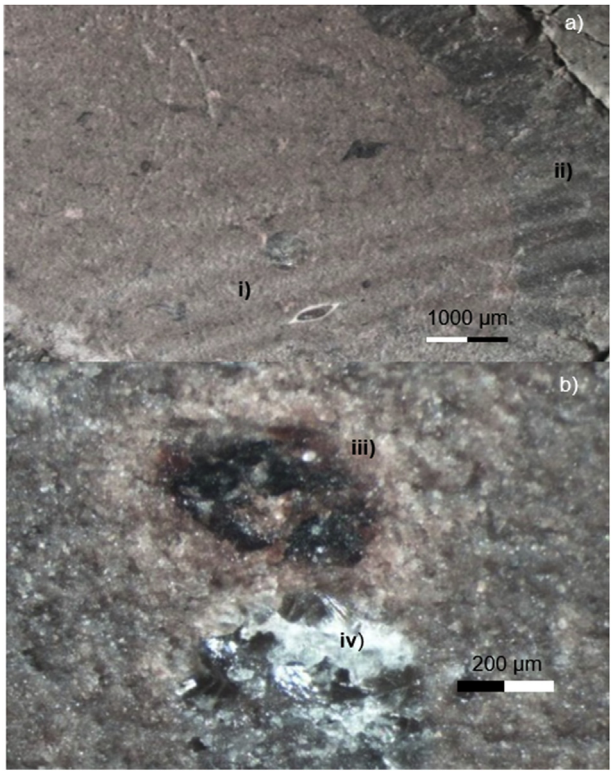

Fig. 8. Examples of carbonate mineralization within a burrow showing rhodochrosite within the center, in this case a) i) diatom has been replaced by rhodochrosite, and ii) calcite or anhydride is present in the exterior (904 mbsf). b) Co-occurring rhodochrosite iii) and barite mineralization iv) in burrow 928 mbsf.

contemporaneous within ongoing deformation but others predate it. Similarly, for the veins there are several instances where there are single slickencrysts (Fig. 7b) indicating single deformation phases, whereas other veins evidence multiple phases of crack and seal (Fig. 7c). However, euhedral crystals are present in some intervals (Fig. 7a), and these are clearly undeformed suggesting a phase of vein-formation that postdates deformation in the underthrust sediments. The co-occurrence and intergrowth of barite and rhodochrosite in burrows, and co-occurrence of barite veins and stratbound mineralization suggest that some phases of stratabound mineralization overlap (Fig. 8).

Barite and rhodochrosite both have densities significantly higher than the formation's bulk density e.g. $> 3.5\ g\ cm^{-3}$ compared to $< 2.5\ g\ cm^{-3}$ (Heuer et al., 2017), and thus anomalous XCT densities can be used to map veins, stratabound patches and the thickness of mineralized intervals (Supplementary Information 2). The thickness of a mineralized interval can be modelled by considering the amount of time that a region spends in a condition of retrograde solubility subsequent to the ingress of hotfluid. This is graphically illustrated in Fig. 3b and c. Very little additional heat is conducted to sediments further than 50 cm from a vein (Fig. 3b) and after 3 days no thermal signature remains and temperatures are significantly reduced after 1 day (Fig. 3c).

There is a good correspondence between our model predictions and the measured thickness of mineralization-anomalies seen in shipboard XCT data (Supplementary Information 2); e.g. and it can be shown that anomalous densities are not observed in regions too distant from a vein to have been heated above precipitation temperatures (Tonai et al., 2019). It appears that the incursion of hydrothermal fluid into the underthrust sediments must be time-limited. Models in which fluid flow was sustained for longer durations predicted alteration halos far larger than observed. This is also supported by biomarker thermal maturity parameters. Although the low-temperature hydrothermal fluid only affected localized areas in the underthrust sediments and is episodic, it may have important implications on the subseafloor biosphere as the temperatures encountered within the aureoles of the veins exceed the upper temperature record (122 °C) of hyperthermophiles grown in

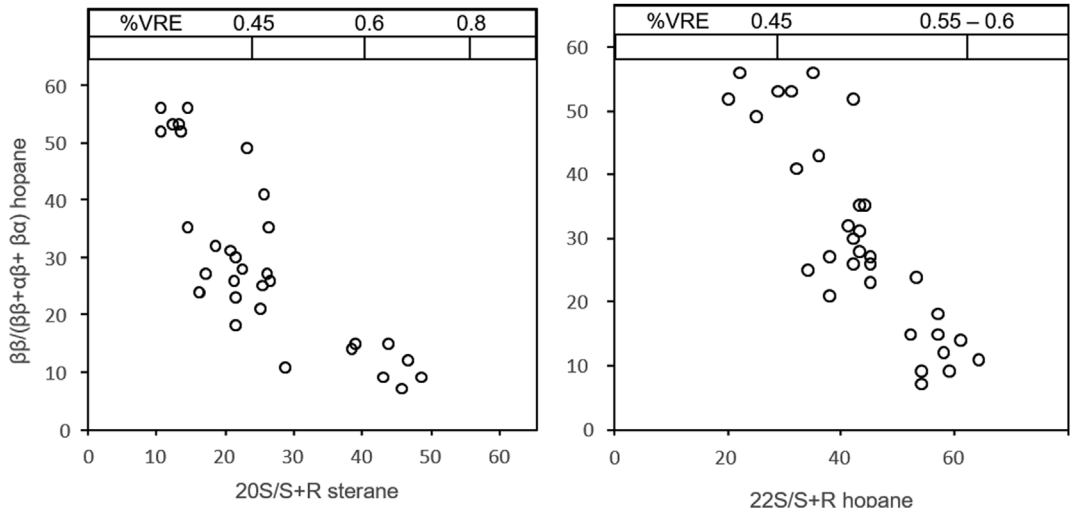

Fig. 9. Thermal maturity cross plot comparing thermal maturity parameters for which there are kinetic models (the 20S sterane and 22S hopane), against the ββ hopane parameter. Vitrinite Reflectance Equivalence is illustrated on the top x-axis (taken from Killops and Killops, 2005). **a)** 20S/S + R sterane calculated as C_{29} 5α,14α,17α(H)20(S) sterane/(C_{29} 5α,14α,17α(H)20(S) + C_{29} 5α,14α,17α(H)20(R) sterane); ββ/(ββ + αβ + βα) = C_{30} 17β,21β(H) hopane/(C_{30} 17β,21β(H) + C_{30} 17α,21β(H) + C_{30} 17β,21α(H) hopane); **b)** ββ/(ββ + αβ + βα) calculated as for a); 17α,21β(H)22(S); 22S/S + R hopane = C_{31} 17α,21β(H)22(S) hopane/(C_{31} 17α,21β(H)22(S) + C_{31} 17α,21β(H)22(R) hopane).

laboratory cultures (Takai et al., 2008).

4.2. Thermal history and thermal anomalies

The sterane % 20S and hopane % 22S parameters both have kinetic models assigned to them based on experimental studies and have been validated in a number of settings (MacKenzie and Craw, 1993). Such models are important because they permit the effects of both duration of heating and temperature to be evaluated and this allows the investigation of the effects of burial diagenesis and heating within the thermal aureole of a mineral vein to be modelled. Excepting the elevated thermal maturities of some samples 800–850 mbsf (as noted earlier), the raise in thermal maturity observed from 890 to 1160 mbsf for the sterane % 20S and hopane % 22S parameters within the zone affected by hydrothermal mineralization can be explained by burial diagenesis and heating at temperatures generally less than 120 °C. This temperature is considerably lower than the pressure-corrected temperatures obtained from fluid inclusions (118–219 °C), therefore biomarker thermal maturity data suggest that sedimentary organic matter in underthrust sediments has not been heated for sufficient duration by the passage of hot fluids to be measurably altered.

Short lived thermal events are commonly recorded within sedimentary basins worldwide, although their context varies. They can be defined as instances where temperature observations (direct measurement, or temperatures obtained from fluid inclusion or fission-track analysis) decouple from temperatures obtained from kinetic-dependent parameters such as virtinite reflectance, smectite-illite and/or opal-quartz conversion or certain biomarker thermal maturity parameters (Parnell, 2010). This decoupling occurs because many kinetic-dependent geochemical proxies require long durations to change at a specified temperature. Specific examples within the temperature ranges encountered at Site C0023 include the Hedeberg group in the central Appalachians (Dorobek, 1989; Machel and Cavell, 1999), the Timor Sea (O'Brien et al., 1996), the UK Atlantic Margin (Parnell, 2010) and the Burgan and Umm Gudair fields in Kuwait (Al-Hajeri et al., 2017). In these cases, hot fluids with temperatures of 200 °C or greater are evidenced or measured in fluid inclusions, etc., but because heating is for durations generally less than 100,000 years, kinetic dependent-parameters evidence little to no alteration (Lampe et al., 2001).

If the heating at Site C0023 was not sufficiently long in time to alter a parameter, it is reasonable to consider how many cycles of heating within the aureole of a vein would be sufficient to bring about a change in thermal maturity, or what temperature might be needed. Fig. 12 illustrates the number of episodes of heating at 180, 270 and 360 °C needed to thermally alter biomarkers within sediments (e.g. repeated exposure to the heating/profile shown in Fig. 3c). For there to be a measurable change in the thermal maturity of organic matter as a consequence of the influx of mineralizing fluids there would have to be many cycles of heating (100's of thousands of such events during the Quaternary) or the fluids much hotter (e.g. much hotter than 300 °C). The temperatures shown in Fig. 10, that could cause changes in thermal maturity (> 300 °C) match those used for the artificial maturation of biomarkers under experimental conditions (Mackenzie et al., 1981, e.g. the model results match laboratory measurements). Consequently, it can be shown that some organic matter at C0023 is thermally mature with respect to the onset of hydrocarbon generation (Fig. 10) because of burial diagenesis and not be because of the passage of hot fluids. Currently the only region presenting a thermal maturity anomaly (measurable in all three biomarker parameters) that cannot be explained by burial diagenesis is at the base décollement.

Despite differences between the models used for Sites C0023 and 1174 (this study and Horsfield et al., 2006), such as the thermal conductivity of sediments and calibrants used for thermal maturity, similar conclusions are drawn. The important conclusions are that the basal section of the Lower Shikoku Basin has been sufficiently heated by burial metamorphism to generate hydrocarbons, and the underthrust sediments need to have experienced a higher heatflow in the geological past to account for the current condition of the sedimentary organic matter. Excursions seen in the three biomarker thermal maturity parameters can be accounted for by normal burial diagenesis and short lived thermal events have little effect on sedimentary organic matter; they would not generate additional petroleum from sedimentary organic matter at depths between 950 and 1112 mbsf. While it is conceivable that multiple episodes of short-lived fluid migration could alter kinetic-based geochemical parameters, there is no evidence for this at Site C0023.

5. Conclusions

The phenomena of hot fluids minimally altering the thermal maturity of kinetic-based parameters, but leaving evidence of its presence in mineral phases has previously been recognized in continental basins

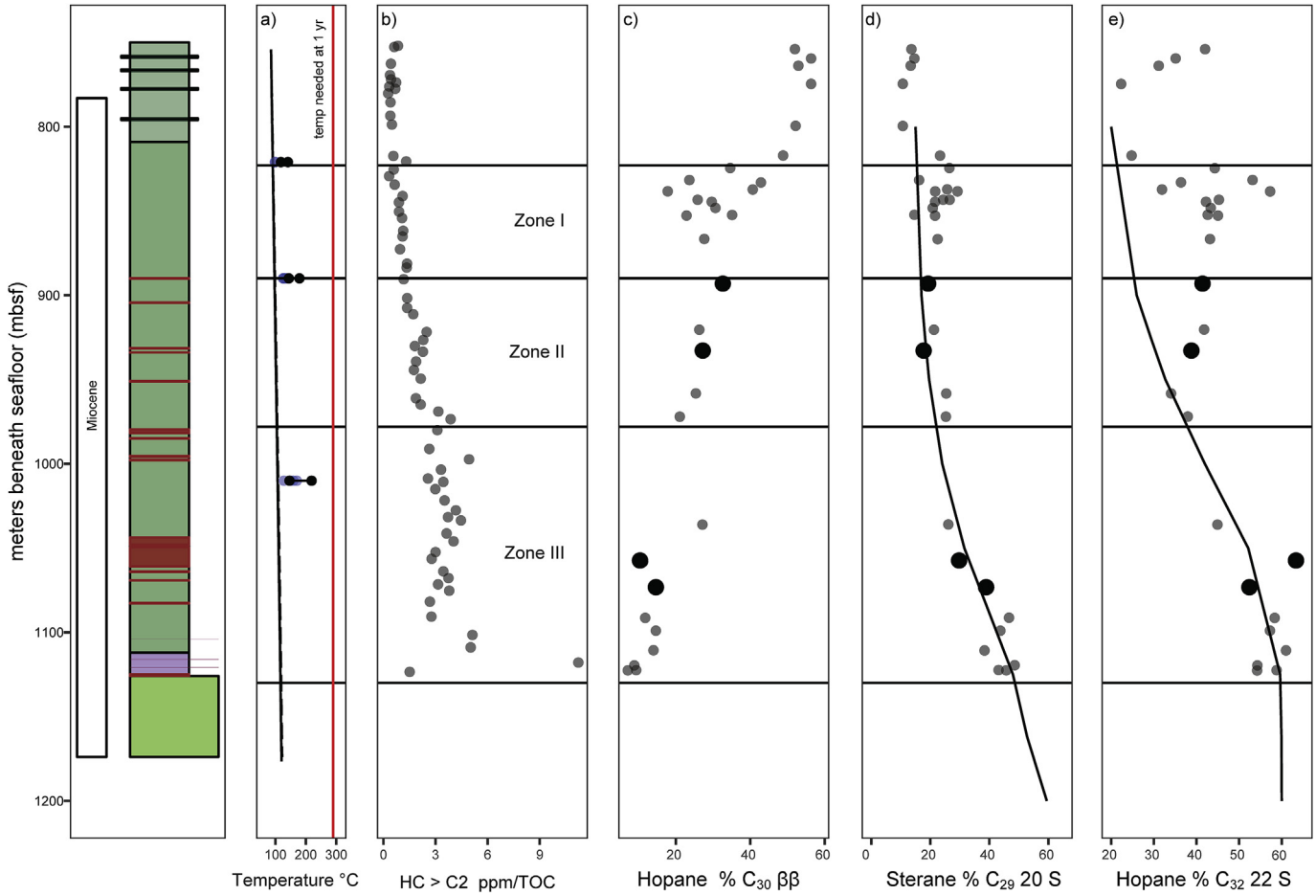

Fig. 10. Downhole plots illustrating the thermal history of C0023 and its impact on burial diagenesis. a) Fluid inclusion temperatures. Blue dots (with vertical jitter applied) = measured fluid inclusion homogenization temperatures; black dumbbells = pressure corrected maximum and minimum trapping temperatures Red line is the temperature needed to raise the 20S sterane and 22S hopane parameters to oil window values in less than 1 year. Black line = present day temperature. b) non-biogeneic light hydrocarbon abundance (ethane, propane, butane), inferred to be the product of petroleum generation (Heuer et al., 2017); c) ββ/(ββ + αβ + βα) calculated as for Fig. 10; d) open circle = 20S/S + R sterane calculated as in Fig. 10, black line prediction of parameter based on burial diagenesis (Mackenzie and McKenzie, 1983); e) ○ = 22S/S + R hopane calculated as in Fig. 9, black line prediction of parameter based on burial diagenesis (Mackenzie et al., 1981). Large filled black circles correspond to samples of mineralized sediment. (For interpretation of the references to color in this figure legend, the reader is referred to the Web version of this article.)

worldwide; the data presented here represents the first instance of the effect being observed in ocean sediments and ocean sedimentary basins. Mineralization assemblages in the underthrust domain formed from low-temperature hydrothermal fluids at IODP Site C0023. Mineralization includes veins and stratabound alteration patches rich in barite and rhodochrosite. The fluid inclusions trapped in barite crystals reveal homogenization temperatures of 98–175 °C and pressure-corrected trapping temperatures of 118–219 °C. This mineralization has no measurable generative effect with respect to hydrocarbons or petroleum generation. The current thermal maturity of organic matter at Site C0023 can mostly be explained by a conventional burial diagenesis, taking account of past tectonic settings.

Statements authorship

MYT: Designed research of this study, wrote and coordinated the MS (co-lead-author). Contribution to database: core description, sample selection, geochemical analyses.

SAB: Designed research of this study, conducted basin modeling, wrote and coordinated the MS (co-lead-author). Contribution to database: core description, sample selection, geochemical analyses.

ZW: Conducted basin modeling and geochemical analyses.

AM: Conducted basin modeling and contributed text to the MS.

ST: Conducted basin modeling, contributed data (core description) and MS text.

DM: Conducted Fluid Inclusion Analysis.

KY: Contributed data (core description) and MS text.

YuY: Contributed to research design and database (core description).

NK: Contributed data (core description) and MS text.

NO: Contributed data (core description) and MS text.

TH: Contributed data (core description) and MS text.

MK: Contributed to research design and database (age control for Base).

FS: Contributed to research design, database (sample selection), and MS text.

AI: Contributed to database (core description, sample selection).

YaY: Contributed to database (age control for Base).

YK: Lead expedition project management and contributed to coordination research plans.

YM: Co-Chief Scientist of IODP Expedition 370, designed and coordinated research plans of the expedition, contributed to MS writing.

FI: Co-Chief Scientist of IODP Expedition 370, designed and coordinated research plans of the expedition, contributed to MS writing.

VBH: Co-Chief Scientist of IODP Expedition 370, designed and coordinated research plans of the expedition, contributed to MS writing.

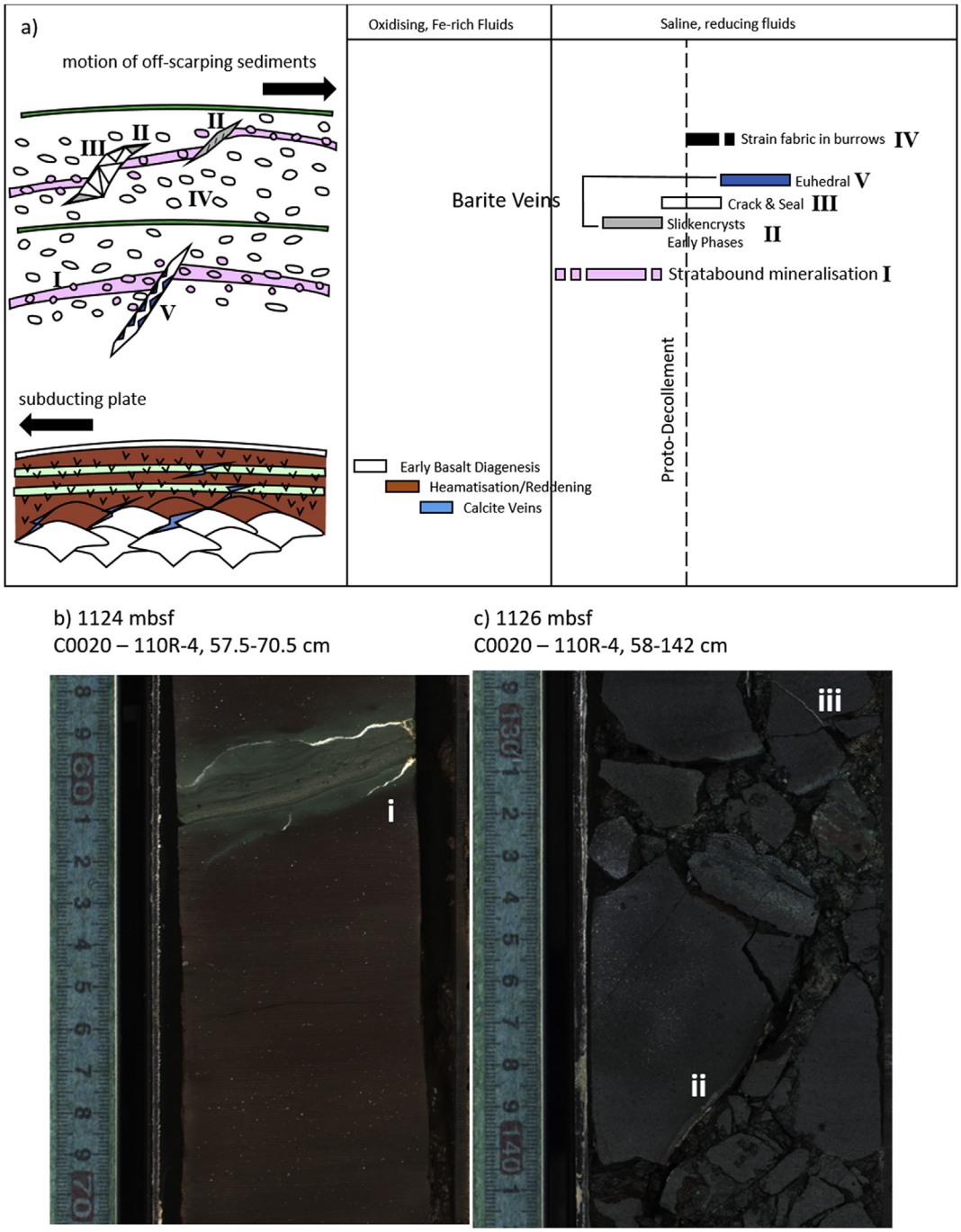

Fig. 11. a) Paragenetic sequence of events for short duration mineralization within underthrust sediments, and its comparison to umbers in the basal section. Relative time on x-axis and relative depth on y-axis. I-IV denotes different stages of mineralization within the underthrust sediments based on vein habits seen in Site C0023. Different stages of mineralization present in sediments overlying basalt are also shown. Redrawn form Heuer et al. (2017). **b)** Core 110R-4. Stratabound heamatization following sedimentary fabrics, and calcite veins near parallel to worm burrows and ichnofabrics. **c)** ii) & iii) Calcite veins in basalt.

KUH: Lead-Proponent of IODP Expedition 370, designed and coordinated research plans of the expedition, discussed scientific ideas of this study, contributed to MS writing.

Acknowledgments

This research used samples and data provided by the International Ocean Discovery Program (IODP). The authors are grateful to the IODP and the Ministry of Education, Culture, Sports, Science and Technology of Japan (MEXT). We thank crew, drilling team, geologists and lab technicians on *D/V Chikyu* and the staff of the Kochi Institute for Core Sample Research for supporting operations. This work was supported by the European Consortium for Ocean Research Drilling (ECORD) research grant [2017 to MYT]; and theNatural Environment Research Council (NERC) grant, UK [NE/P015182/1 2017 to SAB]. ZW acknowledges technical support provided by Colin Taylor at the University of Aberdeen. Petromod 2017 was provided by Schlumberger. VBH and KUH acknowledge funding from the Deutsche Forschungsgemeinschaft through the Cluster of Excellence, "The Ocean Floor – Earth's Uncharted Interface" and Project Grant HE8034/1-1 2019. This is a contribution to the Deep Carbon Observatory.

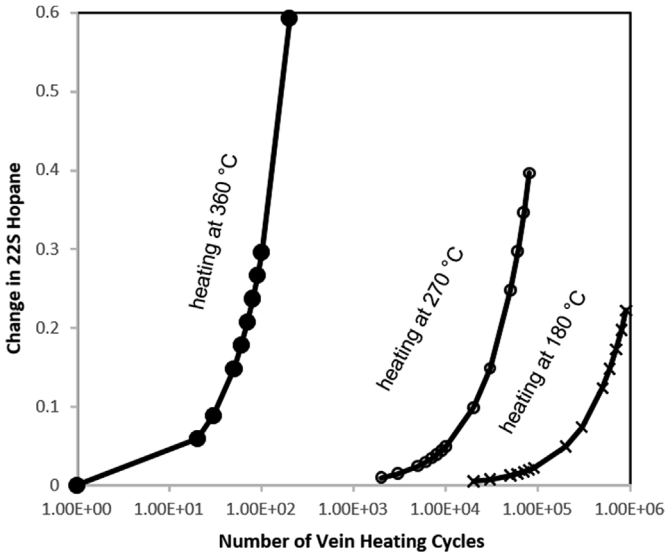

Fig. 12. Graph illustrating the effects of continuously repeated cycles of heating within the aureole of a vein using the hottest cooling curve shown in Fig. 3c. Calculations were made using the model for the 22S/S + R hopane parameter from Mackenzie and McKenzie (1983) and applying a varied number if cycles. Projections are also shown for higher temperature heating with maximum peak temperatures of 270 and 360 °C.

Appendix A. Supplementary data

Supplementary data to this article can be found online at https://doi.org/10.1016/j.marpetgeo.2019.104080.

References

Alexander, J., Pickering, K.T., Bailey, E., 1999. Hydrothermal sediments associated with a relict back-arc centre in the Shikoku Basin, recovered from the Nankai accretionary prism, Japan. Isl. Arc 8, 281–292.

Al-Hajeri, M.M., Parnell, J., Bowden, S., Costanzo, A., Feely, M., 2017. Deep hydrothermal activity in hydrocarbon reservoirs, South Kuwait. Arabian J. Geosciences 10 (2), 41.

Aoki, Y., Tamano, T., Kato, S., 1982. Detailed structure of the Nankai Trough from migrated seismic sections. In: In: Watkins, J.S., Drake, C.L. (Eds.), Studies in Continental Margin Geology: American Association of Petroleum Geologists Special, vol. 34. pp. 309–322.

Athy, L.F., 1930. Density, porosity and compaction of sedimentary rocks. AAPG m. Assoc. Pet. Geol. Bull. 14, 1–24.

Bangs, N.L.B., Moore, G.F., Gulick, S.P.S., Pangborn, E.M., Tobin, H.J., Kuramoto, S., Taira, A., 2009. Broad, weak regions of the Nankai Megathrust and implications for shallow coseismic slip. Earth Planet. Sci. Lett. 284, 44–49.

Blount, C.W., 1977. Barite solubilities and thermodynamic quantities up to 300 °C and 1400 bars. Americal Mineralogist 62, 942–957.

Bonneville, A., Capolsini, P., 1999. THERMIC: a 2-D finite-element tool to solve conductive and advective heat transfer problems in Earth Sciences. Comput. Geosci. 25, 1137–1148.

Bons, P.D., Elburg, M.A., Gomez-Rivas, E., 2012. A review of the formation of tectonic veins and their microstructures. J. Struct. Geol. 43, 33–62.

Bowden, S.A., Walker, J., Ziolkowski, M., Taylor, C., 2016. Data report: bitumen extracted from hydrothermally altered sediments encountered during Expedition 331. In: Takai, K., Mottl, M.J., Nielsen, S.H. (Eds.), Expedition 331 Scientists, Proceedings of the Integrated Ocean Drilling Program, 331. Integrated Ocean Drilling Program Management International, Inc., Tokyo.

Dorobek, S., 1989. Migration of orogenic fluids through the Siluro-Devonian Helderberg Group during late Paleozoic deformation: constraints on fluid sources and implications for thermal histories of sedimentary basins. Tectonophysics 159 (1–2), 25–45.

Driesner, T., Heinrich, C.A., 2007. The system H_2O-NaCl. I. Correlation formulae for phase relations in temperature-pressure-composition space from 0 to 1000°C, 0 to 5000 bar, and 0 to 1 X_{NaCl}. Geochem. Cosmochim. Acta 71 (20), 4880–4901.

Driesner, T., 2007. The system H_2O-NaCl. II. Correlations for molar volume, enthalpy, and isobaric heat capacity from 0 to 1000 degrees C, 1 to 5000 bar, and 0 to 1 X_{NaCl}. Geochem. Cosmochim. Acta 71 (20), 4902–4919.

Farrimond, P., Taylor, A., TelnÆs, N., 1998. Biomarker maturity parameters: the role of generation and thermal degradation. Org. Geochem. 29 (5–7 -7 pt 2), 1181–1197.

Hagino, K., the Expedition 370 Scientists, 2018. Data report: calcareous nannofossils from the middle Miocene to Pleistocene, IODP expedition 370 site C0023. In: Heuer, V.B., Inagaki, F., Morono, Y., Kubo, Y., Maeda, L. (Eds.), The Expedition 370 Scientists, Temperature Limit of the Deep Biosphere off Muroto. Proceedings of the International Ocean Discovery Program, 370, College Station, TX.

Harris, R., Yamano, M., Kinoshita, M., Spinelli, G., Hamamoto, H., Ashi, J., 2013. A synthesis of heat flow determinations and thermal modeling along the Nankai Trough. Jpn. J. Geophy. Res.: Solid Earth 118, 2687–2702. https://doi.org/10.1002/jgrb.50230.

Heuer, V.B., Inagaki, F., Morono, Y., Kubo, Y., Maeda, L., the Expedition 370 Scientists, 2017. Temperature Limit of the deep biosphere off Muroto. In: Proceedings of the International Ocean Discovery Program, 370. International Ocean Discovery Program, College Station, TX.

Hibbard, J.P., Laughland, M.M., Kang, S.M., Karig, D., 1993. The thermal imprint of spreading ridge subduction on the upper structural levels of an accretionary prism, southwest Japan. Special Paper 273 In: Underwood, M.B. (Ed.), Thermal Evolution of the Tertiary Shimanto Belt, Southwest Japan: an Example of Ridge-Trench Interaction. Geological Society of America, pp. 83–101.

Horsfield, B., Schenk, H.J., Zink, K., Ondrak, R., Dieckmann, V., Kallmeyer, J., Mangelsdorf, K., Di Primio, R., Wilkes, H., Parkes, R.J., Fry, J., 2006. Living microbial ecosystems within the active zone of catagenesis: implications for feeding the deep biosphere. Earth Planet. Sci. Lett. 246, 55–69. https://doi.org/10.1016/j.epsl.2006.03.040.

Johnson, H.P., Becker, K., Von Herzen, R., 1993. Near-axis heat flow measurements on the northern Juan De Fuca Ridge: implications for fluid circulation in oceanic crust. Geophys. Res. Lett. 20 1875-187.

Kastner, M., Elderfield, H., Jenkins, W.J., Gieskes, J.M., Gamo, T., 1993. Geochemical and isotopic evidence for fluid flow in the western Nankai subduction zone, Japan. In: In: Hill, I.A., Taira, A., Firth, J.V. (Eds.), Proceedings of the Ocean Drilling Program, Scientific Results, vol. 131. pp. 397–413.

Killops, S., Killops, V., 2005. Introduction to Organic Geochemistry, second ed. Blackwell Publishing, Oxford.

Lampe, C., Person, M., Nöth, S., Ricken, W., 2001. Episodic fluid flow within continental rift basins: some insights from field data and mathematical models of the Rhinegraben. Geofluids 1 (1), 42–52.

MacKenzie, D.J., Craw, D., 1993. Structural control of gold-scheelite mineralisation in a major normal fault system, Barewood. eastern Otago, New Zealand: N. Z. J. Geol. Geophys. 36, 437–445.

Mackenzie, A.S., McKenzie, D., 1983. Isomerization and aromatization of hydrocarbons in sedimentary basins formed by extension. Geol. Mag. 120, 417–470.

Mackenzie, A.S., Lewis, C.A., Maxwell, J.R., 1981. Molecular parameters of maturation in the Toarcian shales, Paris Basin, France-IV. Laboratory thermal alteration studies. Geochem. Cosmochim. Acta 45 (12), 2369–2376.

Mahony, S.H., Wallace, L.M., Miyoshi, M., Villamor, P., Sparks, R.S.J., Hasenaka, T., 2011. Volcano-tectonic interactions during rapid plateboundary evolution in the Kyushu region, SW Japan. Bull. Geol. Soc. Am. 123, 2201–2223.

Machel, H.G., Cavell, P.A., 1999. Low-flux, tectonically-induced squeegee fluid flow ("hot flash") into the Rocky Mountain Foreland Basin. Bull. Can. Petrol. Geol. 47 (4), 510–533.

Midttømme, K., Roaldset, E., 1999. Thermal conductivity of sedimentary rocks: uncertainties in measurement and modelling. In: Muds and Mudstones: Physical and Fluid Flow Properties, vol. 158. Geological Society, London, Special Publications, pp. 45–60.

Moore, G.F., Taira, A., Klaus, A., et al., 2001. Initial Reports, vol. 190 In: Proceedings of the Ocean Drilling Program. Ocean Drilling Program, College Station, TX.

Nadeau, P.H., 2011. Earth's energy "Golden Zone": a synthesis from mineralogical research. Clay Miner. 46, 1–24.

O'Brien, G.W., Lisk, M., Duddy, I., Eadington, P.J., Cadman, S., Fellows, M., 1996. Late Tertiary fluid migration in the Timor sea: a key control on thermal and diagenetic histories? APPEA J. 36, 399–424.

Okino, K., Kato, Y., 1995. Geomorphological study on a clastic accretionary prism: the Nankai Trough. Isl. Arc 4, 182–198.

Parnell, J., 2010. Potential of palaeofluid analysis for understanding oil charge history. Geofluids 10 (1–2), 73–82.

Parnell, J., Bowden, S.A., Osinski, G.R., Lee, P., Green, P., Taylor, C., Baron, M., 2007. Organic geochemistry of impactites from the haughton impact structure, devon island, Nunavut. Canada Geochim. Cosmochim. Acta 71 (7), 1800–1819.

Pisani, P., Reshef, M., Moore, G., 2005. Targeted 3-D prestack depth imaging at Legs 190-196 ODP drill sites (Nankai Trough, Japan). Geophys. Res. Lett. 32. https://doi.org/10.1029/2005GL024191.

Plummer, N.L., Busenberg, E., 1982. The solubilities of calcite, aragonite and vaterite in CO_2-H_2O solutions between 0 and 90 °C, and an evaluation of the aqueous model for the system $CaCO_3$-CO_2-H_2O. Geochem. Cosmochim. Acta 46, l0ll–1040.

Pritchard, H.M., Maliotis, G., 1995. Gold mineralisation associated with cold, off-axis, fluid activity in the Troodos ophiolite Cyprus. J. Geol. Soc. Lond. 155, 223–231.

Robertston, A.H.F., 1975. Cyprus umbers: basalt-sediment relationships on a Mesozoic ocean ridge. J. Geol. Soc. 131, 511–531.

Simoneit, B.R.T., Lonsdale, P.F., 1982. Hydrothermal petroleum in mineralized mounds at the seabed of Guaymas Basin. Nature 295, 198–202.

Sweeney, J., Burnham, A.K., 1990. Evaluation of a simple model of vitrinite reflectance based on chemical kinetics. AAPG Bull. 74 (10), 1559–1570.

Taira, A., Ashi, J., 1993. Sedimentary facies evolution of the Nankai forearc and its implications for the growth of the Shimanto accretionary prism. In: Hill, I.A., Taira, A., Firth, J.V. (Eds.), Proceedings of the Ocean Drilling Program, Scientific Results 131. Ocean Drilling Program, College Station, Texas, pp. 331–341.

Taira, A., Hill, I., Firth, J.V., et al., 1991. In: Proceedings of the Ocean Drilling Program, ScientificResults, 131. Ocean Drilling Program, College Station,TX.

Takai, K., Nakamura, K., Toki, T., Tsunogai, U., Miyazaki, M., Miyazaki, J., Hirayama, H., Nakagawa, S., Nunoura, T., Horikoshi, K., 2008. Cell proliferation at 122°C and

isotopically heavy CH_4 production by a hyperthermophilic methanogen under high-pressure cultivation. Proc. Natl. Acad. Sci. 105 (31), 10949–10954.
Tonai, S., Kubo, Y., Tsang, M.-Y., Bowden, S.A., Ide, K., Hirose, T., Kamiya, N., Yamamoto, Y., Yang, K., Yamada, Y., Morono, Y., Heuer, V.B., Inagaki, F., Expedition 370 Scientists, 2019. A new method for quality control of geological cores by X-ray computed tomography: application in IODP expedition 370. Front. Earth Sci. 7, 117.
Underwood, M.B., Pickering, K.T., Gieskes, J.M., Kastner, M., Orr, R., 1993. Sedimentat geochemistry, clay mineralogy, and diagenesis: a synthesis of data from Leg 131 Nankai Trough. In: Hill, I.A., Taira, A., Firth, J.V. (Eds.), Proceedings of the Ocean Drilling Program, ScientificResults 131. Ocean Drilling Program, College Station,TX, pp. 343–363.
Watson, J.S., Jones, D.M., Swannell, R.P.J., Van Duin, A.C.T., 2002. Formation of carboxylic acids during aerobic biodegradation of crude oil and evidence of microbial oxidation of hopanes. Org. Geochem. 33, 1153–1169.
Wellsbury, P., Goodman, K., Barth, T., Cragg, B.A., Barnes, S.P., Parkes, R.J., 1997. Deep marine biosphere fueled by increasing organic matter availability during burial and heating. Nature 388, 573–576.
Wilkinson, J.J., 2001. Fluid inclusions in hydrothermal ore deposits. Lithos 55, 229–272.
Wolfram, O., Krupp, R.E., 1996. Hydrothermal solubility of rhodochrosite, Mn (II) speciation, and equilibrium constants. Geochem. Cosmochim. Acta 60, 3983–3994.